OPEN ACCESS



Performance of SK-Gd's Upgraded Real-time Supernova Monitoring System

```
Y. Kashiwagi <sup>1</sup>, K. Abe <sup>1,2</sup>, C. Bronner <sup>1</sup>, Y. Hayato <sup>1,2</sup>, K. Hiraide <sup>1,2</sup>, K. Hosokawa <sup>1</sup>, K. Ieki <sup>1,2</sup>, M. Ikeda <sup>1,2</sup>, J. Kameda <sup>1,2</sup>, Y. Kanemura <sup>1</sup>, R. Kaneshima <sup>1</sup>, Y. Kataoka <sup>1,2</sup>, S. Miki <sup>1</sup>, S. Mine <sup>1,3</sup>, M. Miura <sup>1,2</sup>, S. Moriyama <sup>1,2</sup>, Y. Nakano <sup>1</sup>, Y. Nakano <sup>1</sup>
           M. Nakahata<sup>1,2</sup>, S. Nakayama<sup>1,2</sup>, Y. Noguchi<sup>1</sup>, K. Sato<sup>1</sup>, H. Sekiya<sup>1,2</sup>, H. Shiba<sup>1</sup>, K. Shimizu<sup>1</sup>, M. Shiozawa<sup>1,2</sup>,
 Y. Sonoda<sup>1</sup>, Y. Suzuki<sup>1</sup>, A. Takeda<sup>1,2</sup>, Y. Takemoto<sup>1,2</sup>, H. Tanaka<sup>1,2</sup>, T. Yano<sup>1</sup>, S. Han<sup>4</sup>, T. Kajita<sup>2,4,5</sup>, K. Okumura<sup>2,4</sup>, T. Tashiro<sup>4</sup>, T. Tomiya<sup>4</sup>, X. Wang<sup>4</sup>, S. Yoshida<sup>4</sup>, P. Fernandez<sup>6</sup>, L. Labarga<sup>6</sup>, N. Ospina<sup>6</sup>, B. Zaldivar<sup>6</sup>, B. W. Pointon<sup>7,8</sup>, E. Kearns<sup>2,9</sup>, J. L. Raaf<sup>9</sup>, L. Wan<sup>9</sup>, T. Wester<sup>9</sup>, J. Bian<sup>3</sup>, N. J. Griskevich<sup>3</sup>, S. Locke<sup>3</sup>, M. B. Smy<sup>2,3</sup>, H. W. Sobel<sup>2,3</sup>, V. Takhistov<sup>3,10</sup>, A. Yankelevich<sup>3</sup>, J. Hill<sup>11</sup>, M. C. Jang<sup>12</sup>, S. H. Lee<sup>12</sup>, D. H. Moon<sup>12</sup>, R. G. Park<sup>12</sup>, B. Bodur<sup>13</sup>,
         K. Scholberg<sup>2,13</sup>, C. W. Walter<sup>2,13</sup>, A. Beauchêne<sup>14</sup>, O. Drapier<sup>14</sup>, A. Giampaolo<sup>14</sup>, Th. A. Mueller<sup>14</sup>, A. D. Santos<sup>14</sup>, P. Paganini<sup>14</sup>, B. Quilain<sup>14</sup>, R. Rogly<sup>14</sup>, T. Nakamura<sup>15</sup>, J. S. Jang<sup>16</sup>, L. N. Machado<sup>17</sup>, J. G. Learned<sup>18</sup>, K. Choi<sup>19</sup>, N. Iovine<sup>19</sup>, S. Cao<sup>20</sup>, L. H. V. Anthony<sup>21</sup>, D. Martin<sup>21</sup>, N. W. Prouse<sup>21</sup>, M. Scott<sup>21</sup>, A. A. Sztuc<sup>21</sup>, Y. Uchida<sup>21</sup>,
                  V. Berardi<sup>22</sup>, M. G. Catanesi<sup>22</sup>, E. Radicioni<sup>22</sup>, N. F. Calabria<sup>23</sup>, A. Langella<sup>23</sup>, G. De Rosa<sup>23</sup>, G. Collazuol<sup>24</sup>,
F. Iacob<sup>24</sup>, M. Mattiazzi<sup>24</sup>, L. Ludovici<sup>25</sup>, M. Gonin<sup>5</sup>, L. Périssé<sup>5</sup>, G. Pronost<sup>5</sup>, C. Fujisawa<sup>26</sup>, Y. Maekawa<sup>26</sup>, Y. Nishimura<sup>26</sup>, R. Okazaki<sup>26</sup>, R. Akutsu<sup>10</sup>, M. Friend<sup>10</sup>, T. Hasegawa<sup>10</sup>, T. Ishida<sup>10</sup>, T. Kobayashi<sup>10</sup>, M. Jakkapu<sup>10</sup>, T. Matsubara<sup>10</sup>, T. Nakadaira<sup>10</sup>, K. Nakamura<sup>2,10</sup>, Y. Oyama<sup>10</sup>, K. Sakashita<sup>10</sup>, T. Sekiguchi<sup>10</sup>, T. Tsukamoto<sup>10</sup>, N. Bhuiyan<sup>27</sup>,
 G. T. Burton<sup>27</sup>, F. Di Lodovico<sup>27</sup>, J. Gao<sup>27</sup>, A. Goldsack<sup>27</sup>, T. Katori<sup>27</sup>, J. Migenda<sup>27</sup>, R. M. Ramsden<sup>27</sup>, Z. Xie<sup>27</sup>, S. Zsoldos<sup>2,27</sup>, A. T. Suzuki<sup>28</sup>, Y. Takagi<sup>28</sup>, Y. Takeuchi<sup>2,28</sup>, H. Zhong<sup>28</sup>, J. Feng<sup>29</sup>, L. Feng<sup>29</sup>, J. R. Hu<sup>29</sup>, Z. Hu<sup>29</sup>, M. Kawaue<sup>29</sup>, T. Kikawa<sup>29</sup>, M. Mori<sup>29</sup>, T. Nakaya<sup>2,29</sup>, R. A. Wendell<sup>2,29</sup>, K. Yasutome<sup>29</sup>, S. J. Jenkins<sup>30</sup>, N. McCauley<sup>30</sup>, P. Mehta<sup>30</sup>, A. Tarrant<sup>30</sup>, Y. Fukuda<sup>31</sup>, Y. Itow<sup>32,33</sup>, H. Menjo<sup>32</sup>, K. Ninomiya<sup>32</sup>, Y. Yoshioka<sup>32</sup>, J. Lagoda<sup>34</sup>,
P. Mehta<sup>30</sup>, A. Tarrant<sup>30</sup>, Y. Fukuda<sup>31</sup>, Y. Itow<sup>32,33</sup>, H. Menjo<sup>32</sup>, K. Ninomiya<sup>32</sup>, Y. Yoshioka<sup>32</sup>, J. Lagoda<sup>34</sup>, S. M. Lakshmi<sup>34</sup>, M. Mandal<sup>34</sup>, P. Mijakowski<sup>34</sup>, Y. S. Prabhu<sup>34</sup>, J. Zalipska<sup>34</sup>, M. Jia<sup>35,55</sup>, J. Jiang<sup>35,55</sup>, C. K. Jung<sup>35,55</sup>, W. Shi<sup>35,55</sup>, M. J. Wilking<sup>35,55</sup>, C. Yanagisawa<sup>35,55</sup>, M. Harada<sup>36</sup>, Y. Hino<sup>36</sup>, H. Ishino<sup>36</sup>, Y. Koshio<sup>2,36</sup>, F. Nakanishi<sup>36</sup>, S. Sakai<sup>36</sup>, T. Tada<sup>36</sup>, T. Tano<sup>36</sup>, T. Ishizuka<sup>37</sup>, G. Barr<sup>38</sup>, D. Barrow<sup>38</sup>, L. Cook<sup>2,38</sup>, S. Samani<sup>38</sup>, D. Wark<sup>38,39</sup>, A. Holin<sup>40</sup>, F. Nova<sup>40</sup>, S. Jung<sup>41</sup>, B. S. Yang<sup>41</sup>, J. Y. Yang<sup>41</sup>, J. Yoo<sup>41</sup>, J. E. P. Fannon<sup>42</sup>, L. Kneale<sup>42</sup>, M. Malek<sup>42</sup>, J. M. McElwee<sup>42</sup>, M. D. Thiesse<sup>42</sup>, L. F. Thompson<sup>42</sup>, S. T. Wilson<sup>42</sup>, H. Okazawa<sup>43</sup>, S. B. Kim<sup>44</sup>, E. Kwon<sup>44</sup>, J. W. Seo<sup>44</sup>, I. Yu<sup>44</sup>, A. K. Ichikawa<sup>45</sup>, K. D. Nakamura<sup>45</sup>, S. Tairafune<sup>45</sup>, K. Nishijima<sup>46</sup>, A. Eguchi<sup>47</sup>, K. Nakagiri<sup>47</sup>, Y. Nakajima<sup>2,47</sup>, S. Shima<sup>47</sup>, N. Taniuchi<sup>47</sup>, E. Watanabe<sup>47</sup>, M. Yokoyama<sup>2,47</sup>, P. de Perio<sup>2</sup>, S. Fujita<sup>2</sup>, C. Jesús-Valls<sup>2</sup>, K. Martens<sup>2</sup>, K. M. Tsui<sup>2</sup>, M. R. Vagins<sup>2,3</sup>, J. Xia<sup>2</sup>, M. Kuze<sup>48</sup>, S. Izumiyama<sup>48</sup>, R. Matsumoto<sup>48</sup>, M. Ishitsuka<sup>49</sup>, H. Ito<sup>49</sup>, Y. Ommura<sup>49</sup>, N. Shigeta<sup>49</sup>, M. Shinoki<sup>49</sup>, K. Yamauchi<sup>49</sup>, T. Yoshida<sup>49</sup>, R. Gaur<sup>8</sup>, V. Gousy-Leblanc<sup>8,56</sup>, M. Hartz<sup>8</sup>, A. Konaka<sup>8</sup>, X. Li<sup>8</sup>, S. Chen<sup>50</sup>, B. D. Xu<sup>50</sup>, B. Zhang<sup>50</sup>, M. Posiadala-Zezula<sup>51</sup>, S. B. Boyd<sup>52</sup>, R. Edwards<sup>52</sup>, D. Hadley<sup>52</sup>, M. Nicholson<sup>52</sup>, M. O'Flaherty<sup>52</sup>, B. Richards<sup>52</sup>, A. Ali<sup>8,53</sup>, B. Jamieson<sup>53</sup>, S. Amanai<sup>54</sup>, Ll. Marti<sup>54</sup>, A. Minamino<sup>54</sup>, and S. Suzuki<sup>54</sup>
                                                                                                                                                                                   A. Minamino<sup>54</sup>, and S. Suzuki<sup>54</sup>
                                                                                                                                                                            (The Super-Kamiokande Collaboration)
                         <sup>1</sup> Kamioka Observatory, Institute for Cosmic Ray Research, University of Tokyo, Kamioka, Gifu 506-1205, Japan; kasiwagi@km.icrr.u-tokyo.ac.jp
   <sup>2</sup> Kavli Institute for the Physics and Mathematics of the Universe (WPI), The University of Tokyo Institutes for Advanced Study, University of Tokyo, Kashiwa,
                                                                                                                                                                                                                  Chiba 277-8583, Japan
                                                                                          <sup>3</sup> Department of Physics and Astronomy, University of California, Irvine, Irvine, CA 92697-4575, USA
                                                <sup>4</sup> Research Center for Cosmic Neutrinos, Institute for Cosmic Ray Research, University of Tokyo, Kashiwa, Chiba 277-8582, Japan
                                                                                     ILANCE, CNRS-University of Tokyo International Research Laboratory, Kashiwa, Chiba 277-8582, Japan
                                                                                                                <sup>6</sup> Department of Theoretical Physics, University Autonoma Madrid, 28049 Madrid, Spain
                                                                                              Department of Physics, British Columbia Institute of Technology, Burnaby, BC, V5G 3H2, Canada a TRIUMF, 4004 Wesbrook Mall, Vancouver, BC, V6T 2A3, Canada
                                                                                                                                            Department of Physics, Boston University, Boston, MA 02215, USA
                                                                                                   High Energy Accelerator Research Organization (KEK), Tsukuba, Ibaraki 305-0801, Japan Department of Physics, California State University, Dominguez Hills, Carson, CA 90747, USA
                                                                     12 Institute for Universe and Elementary Particles, Chonnam National University, Gwangju 61186, Republic of Korea
                                                                                                                                                     Department of Physics, Duke University, Durham NC 27708, USA
                                                                                                      <sup>14</sup> Ecole Polytechnique, IN2P3-CNRS, Laboratoire Leprince-Ringuet, F-91120 Palaiseau, France
                                                                                                                                                   Department of Physics, Gifu University, Gifu, Gifu 501-1193, Japan
                                                                                            GIST College, Gwangju Institute of Science and Technology, Gwangju 500-712, Republic of Korea
                                                                                                            School of Physics and Astronomy, University of Glasgow, Glasgow, Scotland, G12 8QQ, UK

18 Department of Physics and Astronomy, University of Hawaii, Honolulu, HI 96822, USA
                                                                                                                                                 Institute for Basic Science (IBS), Daejeon, 34126, Republic of Korea
                                                                                         <sup>20</sup> Institute For Interdisciplinary Research in Science and Education, ICISE, Quy Nhon, 55121, Vietnam
                                                                                                                                         Department of Physics, Imperial College London, London, SW7 2AZ, UK
                                                             <sup>22</sup> Dipartimento Interuniversitario di Fisica, INFN Sezione di Bari and Università e Politecnico di Bari, I-70125, Bari, Italy
                                                                                                        Dipartimento di Fisica, INFN Sezione di Napoli and Università di Napoli, I-80126, Napoli, Italy
                                                                                              Dipartimento di Fisica, INFN Sezione di Padova and Università di Padova, I-35131, Padova, Italy
                                                                                                                        INFN Sezione di Roma and Università di Roma "La Sapienza," I-00185, Roma, Italy
                                                                                                                              Department of Physics, Keio University, Yokohama, Kanagawa, 223-8522, Japan
                                                                                                                                          Department of Physics, King's College London, London, WC2R 2LS, UK
                                                                                                                                     <sup>28</sup> Department of Physics, Kobe University, Kobe, Hyogo 657-8501, Japan
                                                                                                                                    <sup>29</sup> Department of Physics, Kyoto University, Kyoto, Kyoto 606-8502, Japan
```

```
^{\rm 30} Department of Physics, University of Liverpool, Liverpool, L69 7ZE, UK
                    Department of Physics, Miyagi University of Education, Sendai, Miyagi 980-0845, Japan
             <sup>32</sup> Institute for Space-Earth Environmental Research, Nagoya University, Nagoya, Aichi 464-8602, Japan
Kobayashi-Maskawa Institute for the Origin of Particles and the Universe, Nagoya University, Nagoya, Aichi 464-8602, Japan
                                     National Centre For Nuclear Research, 02-093 Warsaw, Poland
         Department of Physics and Astronomy, State University of New York at Stony Brook, NY 11794-3800, USA Department of Physics, Okayama University, Okayama, Okayama 700-8530, Japan
         <sup>37</sup> Media Communication Center, Osaka Electro-Communication University, Neyagawa, Osaka, 572-8530, Japan
                                   Department of Physics, Oxford University, Oxford, OX1 3PU, UK
      <sup>39</sup> STFC, Rutherford Appleton Laboratory, Harwell Oxford, and Daresbury Laboratory, Warrington, OX11 0QX, UK
                                   Rutherford Appleton Laboratory, Harwell, Oxford, OX11 0QX, UK
                      <sup>41</sup> Department of Physics, Seoul National University, Seoul 151-742, Republic of Korea
                     <sup>42</sup> Department of Physics and Astronomy, University of Sheffield, S3 7RH, Sheffield, UK
       <sup>43</sup> Department of Informatics in Social Welfare, Shizuoka University of Welfare, Yaizu, Shizuoka, 425-8611, Japan
                       Department of Physics, Sungkyunkwan University, Suwon 440-746, Republic of Korea
                45 Department of Physics, Faculty of Science, Tohoku University, Sendai, Miyagi, 980-8578, Japan
                         Department of Physics, Tokai University, Hiratsuka, Kanagawa 259-1292, Japan <sup>47</sup> Department of Physics, University of Tokyo, Bunkyo, Tokyo 113-0033, Japan
   Department of Physics, Tokyo Institute of Technology, Meguro, Tokyo 152-8551, Japan

49 Department of Physics, Faculty of Science and Technology, Tokyo University of Science, Noda, Chiba 278-8510, Japan
               Department of Engineering Physics, Tsinghua University, Beijing, 100084, People's Republic of China
                                   Faculty of Physics, University of Warsaw, Warsaw, 02-093, Poland
                            Department of Physics, University of Warwick, Coventry, CV4 7AL, UK
                              53 Department of Physics, University of Winnipeg, MB R3J 3L8, Canada
                <sup>54</sup> Department of Physics, Yokohama National University, Yokohama, Kanagawa, 240-8501, Japan
                  Received 2024 March 14; revised 2024 May 4; accepted 2024 May 17; published 2024 July 19
```

Abstract

Among multimessenger observations of the next Galactic core-collapse supernova, Super-Kamiokande (SK) plays a critical role in detecting the emitted supernova neutrinos, determining the direction to the supernova (SN), and notifying the astronomical community of these observations in advance of the optical signal. In 2022, SK has increased the gadolinium dissolved in its water target (SK-Gd) and has achieved a Gd concentration of 0.033%, resulting in enhanced neutron detection capability, which in turn enables more accurate determination of the supernova direction. Accordingly, SK-Gd's real-time supernova monitoring system has been upgraded. SK_SN Notice, a warning system that works together with this monitoring system, was released on 2021 December 13, and is available through GCN Notices. When the monitoring system detects an SN-like burst of events, SK_SN Notice will automatically distribute an alarm with the reconstructed direction to the supernova candidate within a few minutes. In this paper, we present a systematic study of SK-Gd's response to a simulated Galactic SN. Assuming a supernova situated at 10 kpc, neutrino fluxes from six supernova models are used to characterize SK-Gd's pointing accuracy using the same tools as the online monitoring system. The pointing accuracy is found to vary from 3° to 7° depending on the models. However, if the supernova is closer than 10 kpc, SK_SN Notice can issue an alarm with three-degree accuracy, which will benefit follow-up observations by optical telescopes with large fields of view.

Unified Astronomy Thesaurus concepts: Core-collapse supernovae (304); Supernova neutrinos (1666); Particle astrophysics (96)

1. Introduction

The Super-Kamiokande (SK) detector (Fukuda et al. 2003) is a 50,000 m³ water Cherenkov detector with a fiducial volume of 22.5k m³, consisting of a cylindrical stainless steel tank (39.3 m in diameter and 41.4 m in height) lined with photomultiplier tubes (PMTs). It has an optically separated concentric structure with an inner detector (ID) covered with 11,129 PMTs of 50 cm diameter and an outer detector (OD) with 1885 outward-facing 20 cm PMTs. SK observes neutrinos from various sources, searches for proton decay, and searches for exotic particles such as dark matter. One of the vital roles of SK is to detect corecollapse supernova (SN) neutrinos, to determine the direction of

Original content from this work may be used under the terms of the Creative Commons Attribution 4.0 licence. Any further distribution of this work must maintain attribution to the author(s) and the title of the work, journal citation and DOI.

the SN, and to issue an alarm to astronomical observatories for multimessenger observations of the event.⁵⁷ For accurate pointing to the SN, it is essential to extract as many elastic scattering (ES) events $(\nu + e^- \rightarrow \nu + e^-)$ as possible, since the outgoing electron's direction tracks that of the incoming neutrino. These events must be separated from inverse beta decay (IBD) events ($\bar{\nu}_e + p \rightarrow e^+ + n$) that dominate the event rate but whose positron is weakly correlated with the neutrino direction. This can be achieved by tagging the IBD interactions via their emitted neutron, which produces delayed gamma-ray signals after capturing on nuclei in SK and can be used to form a coincidence with the positron. Prior to 2020 neutron capture on hydrogen was used to identify such neutrons with roughly 25% efficiency, but thereafter gadolinium has been dissolved in the detector water to improve the tagging efficiency (SK-Gd project; Abe et al. 2022a, 2024).

The observational importance of neutrinos from SN burst neutrinos lies in the fact that they rarely interact with matter before reaching a terrestrial detector and therefore carry

⁵⁵ also at BMCC/CUNY, Science Department, New York, New York, 10007, USA.

holds also at University of Victoria, Department of Physics and Astronomy, PO Box 1700 STN CSC, Victoria, BC V8W 2Y2, Canada.

From Hereafter, the word "supernova" or "SN" in this paper always means a core-collapse supernova.

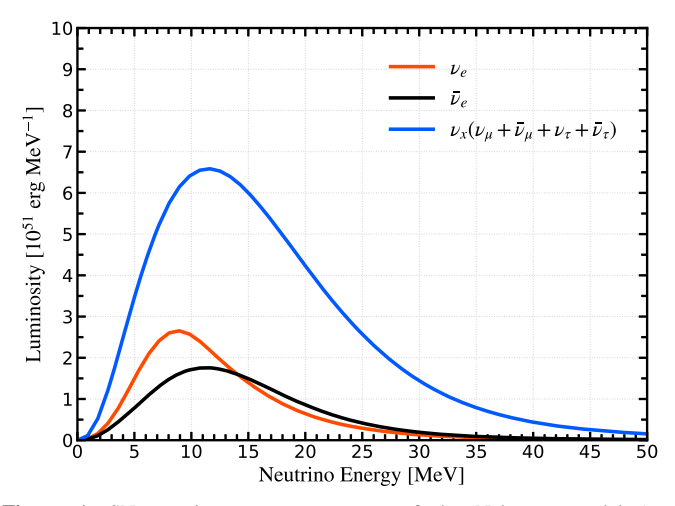


Figure 1. SN neutrino energy spectrum of the Nakazato model (see Section 4.1.2) for each flavor. The red, black, and blue lines represent ν_e , $\bar{\nu}_e$, and $\nu_x (=\nu_\mu + \nu_\tau + \bar{\nu}_\mu + \bar{\nu}_\tau)$, respectively.

information from the dying star at the moment of their production. Figure 1 shows a typical SN neutrino energy spectrum; all the neutrino flavors are emitted, with energies less than $\sim 30 \,\text{MeV}$. Ultimately, SN neutrinos carry 99% of the energy released by the star's gravitational collapse. The neutrino emission process starts shortly before the core's collapse for stars heavier than $10 M_{\odot}$ where M_{\odot} is the total mass of the Sun when the star's silicon shell begins to burn (pre-SN neutrinos; Odrzywolek et al. 2004). When an iron core is formed in the innermost part of the star and fusion stops, gravity induces electron capture $(p + e^- \rightarrow n + \nu_e)$ and photodisintegration of iron nuclei, initiating the core's collapse. The star collapses from within and when the matter at the star's center exceeds nuclear density, the core rebounds against itself (core bounce). Within \sim 0.1 s after the core bounce there is a sharp increase in the number ν_e (neutronization burst), whose observed luminosity typically reaches $\sim 10^{53} \, \mathrm{erg \, s}^{-1}$. The shock wave generated at the core bounce propagates outward but loses energy due to photodisintegration (stagnation of the shock wave). Electromagnetic signatures of the burst become visible when this shock wave regains energy by some mechanism and reaches the photosphere near the stellar surface. Typically, it takes a few hours to a day to blow off the outer stellar layer and produce electromagnetic radiation.⁵⁸ While shock revival is considered to be caused by neutrino heating (e.g., Bethe & Wilson 1985 and Janka 2001), the details of the heating mechanism are still unknown. Several scenarios have been proposed: hydrodynamical mechanisms such as convection (e.g., Herant et al. 1994) and the standingaccretion-shock instability (SASI; e.g., Marek & Janka 2009), acoustic oscillations (e.g., Burrows et al. 2006), and magnetic fields (e.g., Kuroda 2021). As neutrinos are expected to carry information about the explosion mechanism, making their detection during the next SN burst is important. However, SN burst neutrinos have not been observed since their first detection in 1987 (Bionta et al. 1987; Alexeyev et al. 1988).

To understand SK's response to SN in advance and evaluate the performance of SK-Gd's SN monitoring system, it is crucial to simulate SN bursts using SN models. This paper aims to understand the SK's response to Galactic SN systematically and its pointing accuracy (angular resolution) since the start of SK-Gd. We studied SK's response to a simulated SN burst located at a distance of 10 kpc and the pointing accuracy for six SN models considering neutrino oscillations.

This paper is organized as follows. Section 2 summarizes the overview of SK-Gd. In Section 3, we describe the SK-Gd's SN monitoring system. Section 4 explains the SN models used in this paper, simulations for event generation, and detector simulation. In Section 5, we show the simulated SN interaction events for a simulated SN neutrino burst located at 10 kpc using several SN neutrino emission models and their SK-Gd's response. The performance of the SK-Gd's real-time SN monitoring system including pointing accuracy is presented in Section 6 before concluding in Section 7.

2. SK-Gd

2020, ultrapure gadolinium sulfate octahydrate (Gd₂ (SO₄)₃ · 8H₂O) was added to SK's ultrapure water target marking the start of the SK-Gd phase of operations (Abe et al. 2022a). The motivation, as originally posed in Beacom & Vagins (2004), is to enhance SK's ability to detect neutrons due to Gd's large neutron-capture cross section, 254,000 barn for 157Gd compared to 0.33 barn for a proton, followed by the deexcitation emission of 8 MeV in gamma-rays, which is easier to detect than the 2.2 MeV emitted following neutron capture on a proton. During the initial Gd loading, from July to August in 2020, a total concentration of 0.011% Gd was added to the detector, resulting in a neutron-capture efficiency of 50%. From 2022 May to July the concentration was increased to 0.033%, resulting in a 75% capture efficiency (Abe et al. 2022a, 2024). This increased efficiency is expected to improve SK's sensitivity to the diffuse supernova neutrino background (DSNB) as well as its accuracy for locating a nearby SN using the neutrino signal.

There are four channels for SN neutrino interaction in water Cherenkov detectors: inverse beta decay (IBD), elastic scattering (ES), charged current interactions on oxygen (hereafter denoted ¹⁶O CC), such as

$$\nu_{\rm e} + {}^{16}{\rm O} \rightarrow {\rm e}^{-} + {}^{16}{\rm F}$$
 (1)

$$\overline{\nu}_{e} + {}^{16}\text{O} \rightarrow e^{+} + {}^{16}\text{N},$$
 (2)

and neutral current interactions on oxygen (hereafter ¹⁶O NC), such as

$$\nu + {}^{16}\text{O} \rightarrow \nu + {}^{16}\text{O}^*$$
 (3)

$$^{16}\mathrm{O}^* \to ^{15}\mathrm{N} + \mathrm{p} + \gamma \tag{4}$$

$$^{16}\text{O}^* \to ^{15}\text{O} + \text{n} + \gamma$$
 (5)

(Kolbe et al. 2002). Figure 2 shows the relevant cross section as a function of neutrino energy. As can be seen in the figure, IBD interactions dominate in the energy region below ~30 MeV, accounting for about 90% of SN neutrino events in SK. The outgoing positron from these interactions is isotropically emitted, providing little correlation with the incoming neutrino direction. By contrast, ES interactions account for only about 5% of the expected events in SK, but as a forward-scattering process, ES interactions provide a tight correlation with the neutrino direction. At around ~20 MeV the inelastic interactions on oxygen, ¹⁶O CC and ¹⁶O NC, overtake the ES cross section. About 30% of ¹⁶O CC interactions are expected to be observed with a delayed neutron-capture signal, because the resulting

 $[\]overline{^{58}}$ The time becomes shorter if the collapsing star is a Wolf–Rayet star with no hydrogen layer.

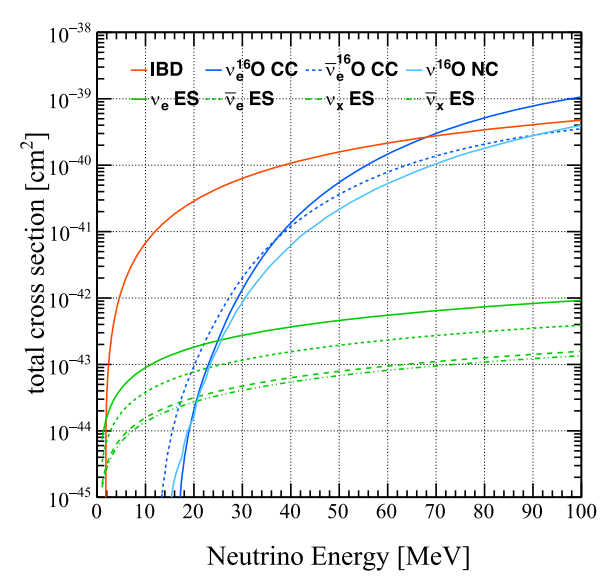


Figure 2. Cross sections for neutrino interactions in water as a function of neutrino energy. The solid red line represents IBD and the green lines represent ES for $\nu_{\rm e}$ (solid), $\bar{\nu}_{\rm e}$ (dotted), ν_{x} (dashed), and $\bar{\nu}_{x}$ (dotted–dashed). The solid blue and dashed blue lines stand for ¹⁶O CC interactions of $\nu_{\rm e}$ and $\bar{\nu}_{\rm e}$, respectively. The dotted–dashed light-blue line indicates ¹⁶O NC interactions. Cross sections are calculated according to Strumia & Vissani (2003) for IBD, Bahcall et al. (1995) for ES, Suzuki et al. (2018) and Nakazato et al. (2018) for ¹⁶O CC interactions, and Langanke et al. (1996) and Kolbe et al. (2002) for ¹⁶O NC interactions.

excited nucleus (¹⁶F and ¹⁶N) may emit one or two neutrons together with gamma-rays (typically 5–9 MeV). Further, the reaction (5) is also expected to be accompanied by neutron capture. In both cases, these neutron captures may cause these interactions to be misidentified as IBD.

3. Real-time Supernova Monitoring System

SK's real-time SN monitoring system, SNWATCH (Abe et al. 2016b), monitors events in the detector to detect SN-like event bursts. Upon SNWATCH's detecting such a burst, SK_SN Notice, SK's SN warning system working together with SNWATCH, issues a prompt warning to astronomical networks as the first alarm of an SN-like event occurrence. SNWATCH determines its direction, and then SK SN Notice broadcasts an announcement of an SN-burst-like detection together with this reconstructed direction and the expected pointing accuracy to astronomical networks. Figure 3 outlines the flow of SNWATCH. To announce the reconstructed SN direction with the best possible pointing accuracy, SNWATCH needs to identify every interaction channel to extract ES events' SN direction sensitivity as much as possible. However, there is a trade-off between accuracy and the time it takes to issue the alarm. Prioritizing accuracy would increase the time to the alarm issue, making it impossible to fulfill the role of SK, which is to detect neutrinos at the very early stages of an SN to enable observations of the optical burst from the beginning to the end. Therefore, to reduce the time to the alert as much as possible, SNWATCH prioritizes identifying "IBD-like" events for extracting "ES-like" events at the expense of pointing accuracy. To identify "IBD-like" events, SNWATCH uses delayed coincidence between IBD events and the following neutron-capture events on protons and Gd. Identifying a positron emission event in an IBD event and the following neutron-capture event is called IBD tagging. In this section, we

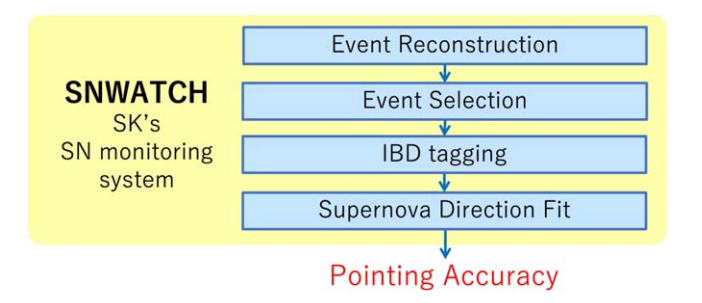


Figure 3. Overview of SK's real-time SN monitoring system, SNWATCH. When an SN-like event burst is detected, SNWATCH performs event reconstruction, event selection, and IBD tagging (see Section 3.1), before applying SN direction fit (see Section 3.2). The resulting reconstructed SN direction is announced with the expected pointing accuracy to astronomical networks (see Section 3.3).

Table 1
Conditions for "Prompt" Candidates and "Delayed" Candidates

Conditions for "Prompt" Candidates	Conditions for "Delayed" Candidates
E > 7 MeV	E < 10 MeV
$g_t^2 \geqslant 0.4$ Number of PMT hits <500	$g_t^2 - g_p^2 > 0$ Within the fiducial volume
Number of PMT lifts < 500 N/S ≤ 0.4	Not a "prompt" candidate
$d_{\text{wall}} > 200 \text{ cm}$	
LE- or HE-triggered event	
Not an OD triggered event	•••

Note. E is the reconstructed energy. Terms g_t^2 and g_p^2 represent the PMT timing goodness and the PMT hit pattern goodness, respectively. N/S ratio is the ratio between the number of low-charge PMT hits (below single photo-electron level) and the total number of PMT hits (Hosaka et al. 2006). LE trigger and HE trigger represent software triggers with ID PMT hit thresholds of 49 and 52, respectively, and OD trigger is set at 22 OD PMT hits. Term d_{wall} is the distance between the reconstructed vertex and the inner detector walls.

describe the flow of SNWATCH: current event reconstruction, selection, and IBD tagging in Section 3.1, the SN direction determination updated to use information from SK-Gd in Section 3.2, and its pointing accuracy and the alarm issue in Section 3.3.

3.1. Event Reconstruction, Selection, and IBD Tagging

SNWATCH uses a custom online version of the standard SK event reconstruction program (Abe et al. 2022b, 2016a) to identify events and reconstruct their vertex position, direction, and total energy. It differs from the standard program due to the need for a fast real-time reconstruction: it uses a simpler and faster muon reconstruction algorithm. It uses preliminary calibration values to compute PMT hit times and charges. This program reconstructs every event detected in the SN-like event bursts, including SN neutrino interactions (IBD, ES, ¹⁶OCC, and ¹⁶O NC) and neutron-capture events. After reconstruction, SNWATCH concentrates on identifying "IBD-like" events as fast as possible to extract "ES-like" events using IBD tagging, as explained in Section 3. To utilize delayed coincidence in performing IBD tagging, SNWATCH divides reconstructed events according to their reconstructed energy into two samples: "prompt" candidates, such as IBD positrons or ES electrons, and "delayed" candidates, i.e., "neutron-capture" candidates. We call this event selection. The conditions for

"prompt" candidates $\overline{\nu}_e$ e^+ "delayed" candidates

Figure 4. Schematic illustration of IBD-tagging algorithm used in SNWATCH. Every possible pair of "prompt" and "delayed" candidates with time difference $\Delta T < 500~\mu s$ and spatial difference $\Delta R < 300~cm$ is tested, and the pair with the smallest ΔR is selected as an IBD candidate.

"prompt" candidates and "delayed" candidates are listed in Table 1. In the selection of "prompt" candidates, three software triggers that store the data within the time window from -5 to $+35~\mu s$ around the triggered time are relevant: low-energy (LE) trigger and high-energy (HE) trigger with the threshold of ID PMT hits of 49 and 52, respectively, and OD trigger, for which the threshold is set at 22 OD PMT hits.

Next, SNWATCH searches for IBD-like interactions, pairing "prompt" candidates with "delayed" candidates based on differences in their trigger times and the spatial separation of their reconstructed vertices. This process is called IBD tagging and is illustrated in Figure 4. The algorithm was designed to be fast and simple. Each possible pair of "prompt" and "delayed" candidates with a trigger time difference $\Delta T < 500 \,\mu s$ and a vertex separation $\Delta R < 300$ cm are tested and the pair with the smallest spatial distance is selected as an IBD candidate. This algorithm provides a tagging efficiency $46.86 \pm 0.04\%$ of IBD interactions and results in a $98.82\% \pm 0.01\%$ sample purity as is discussed below in Section 6.1. Hereafter, we label "prompt" events that have been tagged as an IBD candidate as "IBDlike" and otherwise as "ES-like." Separating these two event samples improves SNWATCH's accuracy for determining the direction to an SN as described in the following Section 3.2.

3.2. SN Direction Fit Algorithm

Though the neutrino direction itself cannot be known directly, the detected recoil electrons of ES can be utilized to reconstruct the SN direction since the outgoing lepton preserves the neutrino's direction, as mentioned in Section 2. Accordingly, it is essential to collect as many ES events as possible. Since ES-like events have high ES purity, separating them from IBD-like events is effective in improving the accuracy of the SN direction determination.

SNWATCH uses a maximum-likelihood (ML) fit to extract the SN direction. An unbinned likelihood taken over all events

$$\mathcal{L} = \exp\left(\sum_{k,r} N_{r,k}\right) \prod_{i} L_{i} \tag{6}$$

is constructed. Here, $N_{r,k}$ is the number of events of the interaction r in the kth energy bin. We note that the indexes r and k are the same as those described in detail in Section 3.1 of Abe et al. (2016b). The index r stands for the type of neutrino interaction, i.e., r = IBD, ES of ν_e , ES of other neutrino flavors, or $^{16}\text{O CC}$ interactions. The index k running from 1 to 5 represents the bin of the reconstructed energy E of the "prompt" candidates in the unit of MeV: $7 \le E < 10$, $10 \le E < 15$, $15 \le E < 22$, $22 \le E < 35$, and $35 \le E < 50$, respectively.

 \hat{L}_i in Equation (6) is a likelihood function for *i*th event, defined as

$$L_i = \sum_r N_{r,k} t_r(f_i) p_r(E_i, \, \hat{d}_i; \, \hat{d}_{SN}^{reco}). \tag{7}$$

Compared to the likelihood function described in Abe et al. (2016b), a term $t_r(f_i)$ has been added. This term is defined according to the IBD flag f_i of *i*th event and the reaction r as:

$$t_{r=\mathrm{IBD}}(f_i) = \begin{cases} \text{IBD tagging efficiency} & (f_i = \mathrm{TRUE}) \\ 1 - (\mathrm{IBD tagging efficiency}) & (f_i = \mathrm{FALSE}) \end{cases}$$
(8)

$$t_{r \neq \text{IBD}}(f_i) = \begin{cases} 0 & (f_i = \text{TRUE}) \\ 1 & (f_i = \text{FALSE}). \end{cases}$$
 (9)

 $p_r(E_i, \hat{d}_i; \hat{d}_{\rm SN}^{\rm reco})$ indicates a probability density function (PDF) for interaction r as a function of the energy E_i and an inner product of $\hat{d}_{\rm SN}^{\rm reco} \cdot \hat{d}_i = \cos\theta_{\rm SN}^{\rm reco}$. E_i is the total electron energy of ith event and uniquely identifies the index k. Term \hat{d}_i is the reconstructed direction of the ith event and $\hat{d}_{\rm SN}^{\rm reco}$ is the SN direction we would like to determine. In the determination of the PDF, SNWATCH utilizes the SK Monte Carlo (MC) simulations (described in Section 4.2): the generated MC samples are divided into 1 MeV bins from 7 to 35 MeV and a combined energy bin greater than 35 MeV. Next, using the known true SN direction $\hat{d}_{\rm SN}^{\rm true}$ illustrated in Figure 5 and a model function, $\cos\theta_{\rm SN}=\hat{d}_{\rm SN}^{\rm true}\cdot\hat{d}_i^{\rm MC}$, the distribution of the generated MC samples is fitted, where $\hat{d}_i^{\rm MC}$ indicates the ith event direction of a generated MC sample.

3.3. Supernova Warning with Direction Information

SNWATCH's alarm is based on two variables: the number of events in a 20 s time window opened behind the time of each reconstructed event ($N_{\rm cluster}$) and a parameter that characterizes the spatial distribution of vertices (D). SNWATCH issues a golden alarm when $N_{\rm cluster} \geqslant 60$ and D=3, indicating the vertices are uniformly distributed ("volume-like"; see Abe et al. 2016b for details). The alarm then provides information about the burst candidate, including the number of observed neutrinos, the duration of the neutrino burst, the GPS-based time stamp of the beginning of the burst, and the estimated SN direction with its uncertainty (i.e., pointing accuracy) in equatorial coordinates.

 $[\]overline{^{59}}$ The division of the four interactions represented by the index r, introduced in Abe et al. (2016b), does not correspond to the division of the four interaction channels described in Section 2, but the likelihood in the current SNWATCH still uses this division of r.

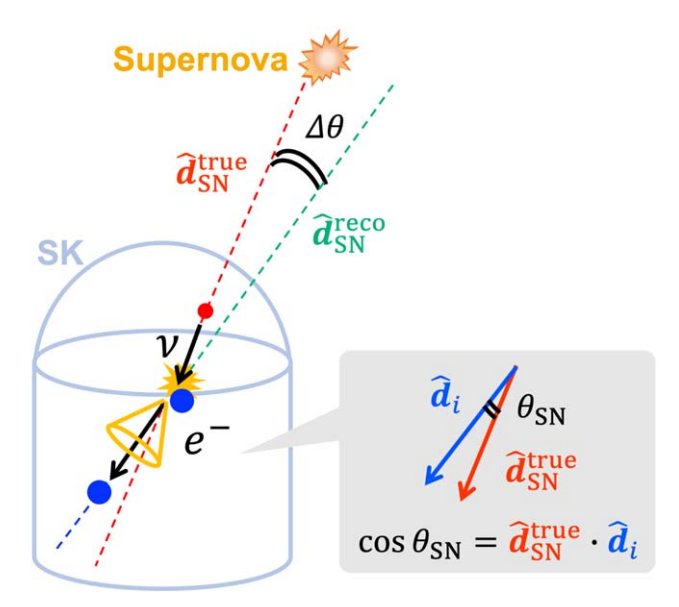


Figure 5. Schematic illustration of $\theta_{\rm SN}$ and $\Delta\theta$. Term $\theta_{\rm SN}$ is the angle between *i*th event direction in SK \hat{d}_i (the blue arrow in the gray box) and the true SN direction $\hat{d}_{\rm SN}^{\rm true}$ (~SN neutrino arrival direction; the red arrow in the gray box). An ES event is illustrated as an example. The direction of the recoil electron corresponds to \hat{d}_i . By applying a maximum-likelihood fit to the distribution of $\cos\theta_{\rm SN}$, the reconstructed SN direction $\hat{d}_{\rm SN}^{\rm reco}$ (the green dashed line) that we would like to determine is obtained in one set of MC samples. Term $\Delta\theta$ is the angle difference between $\hat{d}_{\rm SN}^{\rm reco}$ and $\hat{d}_{\rm SN}^{\rm true}$ and is used to estimate pointing accuracy (see Section 3.3).

Pointing accuracy in SNWATCH indicates the performance of determining the SN direction. To estimate the pointing accuracy in an SN model–independent way, SNWATCH uses a 15×15 resolution matrix with each matrix element containing 3000 MC samples as described in Abe et al. (2016b). SK-Gd aims to realize the SN direction pointing with the accuracy of $\sim 3^{\circ}$ for SN bursts located at 10 kpc, which allows the follow-up observation with large telescopes such as Subaru and the Large Synoptic Survey Telescope (LSST; Nakamura et al. 2016).

An improved SN warning system at SK, SK_SN Notice, 60 started on 2021 December 13 and its alarms can now be received through GCN (General Coordinates Network) Notices 61 (Barthelmy et al. 2000) and are generated in a machine-readable format. If an SN signal is sufficiently large, an alarm will be automatically published within some minutes of detecting the neutrino burst. Signals with a lower significance generate an alarm after undergoing a cross check by analyzers within ≤1 hr. SK_SN Notice can be received through the same framework as other GCN Notices: gamma-ray bursts, gravitational waves, and high-energy neutrino alarms. A dummy (test) alarm is published as a test on the first day of every month.

Based on SNWATCH's alarm, SK also issues warnings on several networks, currently being SNEWS 1.0 (SuperNova Early Warning System 1.0; Antonioli et al. 2004; Scholberg 2008), IAU CBAT (International Astronomical Union Central Bureau for Astronomical Telegrams), ⁶² and ATEL (The Astronomer's telegram; Rutledge 1998) ⁶³. SNWATCH has been running since 1996, and no golden alarm has been sent so far.

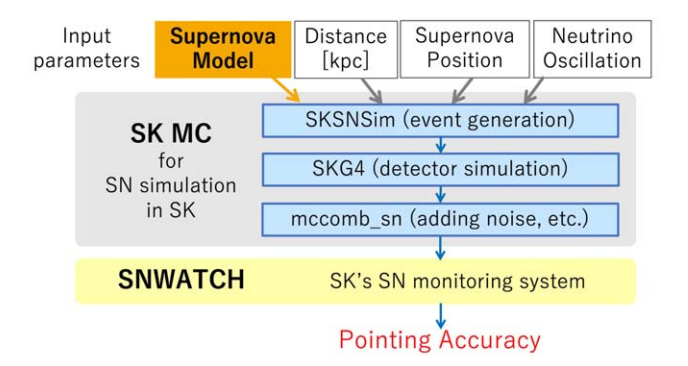


Figure 6. Overview of SN simulation in SK. SN neutrino emission data produced by an SN model (Section 4.1), a distance to the SN, a position of the SN, and a neutrino oscillation scenario (no oscillation, oscillation with normal mass ordering (NMO), or oscillation with inverted mass ordering (IMO)) are input into the SK's event generator, SKSNSim (Section 4.2). The simulated SN neutrino events in SK-Gd are generated with SKSNSim. Then they are processed with SK's detector simulation, SKG4, and mccomb_sn (Section 4.3). SNWATCH processes the events before applying SN direction fit as described in Section 3. Pointing accuracy is estimated by repeating these sets of simulations 3000 times per combination of an SN model, an SN distance, an SN position, and an oscillation type.

The time between the detection and the alarm issue is limited by the processing time of (1) event reconstruction, (2) SN direction fit, and (3) announcement. So far, (1) and (3) have been reduced to less than one minute; however, (2) still takes \sim 5 minutes for an SN located at 10 kpc with the current maximum-likelihood fitter. A new direction fitter is under development for a faster alarm (within less than 1 minute from the SN neutrino burst detection in SK).

4. Simulations

Since the rate of core-collapse SNe in the Galaxy is low, the only way to study the SK detector response to an SN burst is to use simulations. Figure 6 shows the flow of the SK SN simulation. First, we choose an SN model (see Section 4.1), the distance to and the Galactic coordinates of the SN, and neutrino oscillation parameters as input to our event generator, SKSNSim (see Section 4.2). The output of SKSNSim is then given to the SK detector simulation, SKG4, before noise from random trigger data in the actual detector is added to the events via the mccomb_sn process. It additionally applies software triggers (see Section 4.3) to produce a simulated set of events with the same characteristics as the SK data. Finally, SNWATCH reconstructs these events, determines the direction of the SN, and estimates the pointing accuracy (explained in Section 3). Note that this offline analysis uses the same software as the online version SNWATCH. The details of these processes are described below.

4.1. Supernova Models

Since SN burst simulations consume considerable computational resources, models often simulate only the first $\sim 1 \, \mathrm{s}$ post bounce (e.g., Marek & Janka 2009). However, the typical SN neutrino emission timescale is known to be $\sim 10 \, \mathrm{s}$ based on observations of SN1987A, indicating that long-time simulations are also necessary. To overcome computational resource limitations, SN burst neutrino emission simulations impose simplified assumptions and approximations on the physics involved, such as employing one-dimensional spherically symmetric simulations. In many one-dimensional simulations

https://gcn.nasa.gov/missions/sksn

⁶¹ https://gcn.nasa.gov

⁶² http://www.cbat.eps.harvard.edu/

⁶³ http://www.astronomerstelegram.org/

 Table 2

 Summary of Six SN Model Data Employed in This Article

Model Name	Wilson	Nakazato	Mori	Hüdepohl	Fischer	Tamborra
Dimension	1D	1D	1D	1D	1D	3D
Progenitor mass (M_{\odot})	20	20	9.6	8.8	8.8	27
Start time (s)	0.03	-0.05	-0.256	-0.02	0.0	0.011
Duration (s)	14.96	20.05	19.95	8.98	6.10	0.54
EoS	•••	Shen	DD2	Shen	Shen	LS

Note. Shen, DD2, and LS mean equation of state (EoS) by Shen et al. (1998, 1998), EoS based on density-dependent relativistic mean-field model (Hempel & Schaffner-Bielich 2010), and EoS by Lattimer & Swesty (1991), respectively. Note that the start times and the durations shown in the table are after the linear extrapolation described in Appendix A.1 and do not necessarily correspond to that of the published models.

the shock wave does not revive and results in a failed explosion. Such models therefore assume shock revival mechanisms or artificially enhance neutrino reaction rates in order to produce a successful explosion (see Section 4.1.5, for example). Changing these mechanisms, the progenitor mass and equation of state (EoS) contribute to a diversity of SN models. These comments extend to higher-dimensional simulations as well. Indeed, different assumptions on the neutrino heating process and the star's physical parameters, such as its mass and metallicity, as well as different assumptions on the EoS, result in a wide range of models producing flux predictions over both short and long times. Burrows (2013) presents a review of many of the available models. However, to capture all the features of the observed data in SK, to study its response to different models, and to demonstrate our capability to differentiate between them, we focus in this work on SN models with long simulation times.

We selected the following five relatively long-term onedimensional SN models: the historically significant Wilson model (see Section 4.1.1), two long-term one-dimensional models (the Nakazato model and the Mori model; see Section 4.1.2 and Section 4.1.3, respectively), and two electron-capture SN models (the Hüdepohl model and the Fischer model; see Section 4.1.4 and Section 4.1.5, respectively). We also study the Tamborra model, a pioneering threedimensional model (see Section 4.1.6), though it has a comparatively short simulation time, since the other models are all one dimensional. Table 2 summarizes the main characteristics of the six models above. The time evolution of each neutrino flavor's luminosity and mean energy for these models over the first $\sim 0.1 \, \mathrm{s}$ and over the whole time range (20 s) are shown in Figures 7 and 8, respectively. The following subsections summarize each model.

4.1.1. The Wilson Model

The Wilson model (Totani et al. 1998; also called "the Livermore model") is a one-dimensional core-collapse SN model with a long duration, stretching from the start of the collapse to \sim 18 s after the core bounce, which was a pioneering work in the 1990s. Though it is now dated and no longer preferred in the literature, it remains a baseline reference in SN model papers today (Abe et al. 2016b, 2021). It is based on a numerical simulation code developed by Wilson and Mayle (Wilson et al. 1986; Mayle et al. 1987), and with a $20M_{\odot}$ progenitor it can reproduce SN1987A's light curve. In this article, data scanned from Figure 1 of Totani et al. (1998) are used in our simulations, covering neutrino emission up to 15 s after the core bounce.

4.1.2. The Nakazato Model

The Nakazato model (Nakazato et al. 2013) is a long-time one-dimensional model that includes eight sets of progenitor masses and metallicities (four masses, 13, 20, 30, $50\,M_\odot$, and two metallicities, Z=0.02, 0.004). The simulation realizes neutrino emission from the start of the collapse to 20 s after the core bounce by combining a general relativistic neutrino-radiation hydrodynamic simulation (ν RHD) for the early phase and quasi-static evolutionary neutrino diffusion calculations for the PNS cooling phase. This model uses the Shen EoS (Shen et al. 1998, 1998) and makes use of three times (100, 200, and 300 ms after the bounce) for the possible shock revival time. We focus on the $20\,M_\odot$, Z=0.02 (solar metallicity) progenitor model with a shock revival at 200 ms after the bounce in this article. Hereafter, "the Nakazato model" refers to this case.

4.1.3. The Mori Model

The Mori model (Mori et al. 2021) is a one-dimensional core-collapse SN model with a $9.6\,M_\odot$ progenitor that simulates neutrino emission from the onset of core collapse through the PNS cooling phase up to 20 s after the core bounce. It uses a general relativistic hydrodynamics code with a spherically symmetric geometry for the accretion phase known as GR1D (O'Connor 2015) to cover the PNS cooling phase. This model employs an EoS based on the density-dependent relativistic mean field (DD2; Mori et al. 2021).

4.1.4. The Hüdepohl Model

The Hüdepohl model (Hüdepohl et al. 2010) is a onedimensional electron-capture SN model with a spherically symmetric geometry. An $8.8 M_{\odot}$ progenitor with an O-Ne-Mg core modeled by Nomoto (1987) is adopted. The simulation was performed using the neutrino-radiation hydrodynamics code PROMETHEUS-VERTEX, which is composed of the hydrodynamics solver PROMETHEUS (Fryxell et al. 1991) and the neutrino transport code VERTEX (Rampp & Janka 2002). Shen's EoS (Shen et al. 1998, 1998) is used. For the set of neutrino interactions, the model considers two cases: the Sf case with a "full" set of neutrino interactions listed in Appendix A in Buras et al. (2006) and the Sr case with a "reduced" set of neutrino interactions omitting pure neutrino interactions listed in Bruenn (1985). We use the results of the Sf case in this article, referred to as "the Hüdepohl model" hereafter. This case covers the PNS cooling phase but has a shortened simulation period lasting up until ~ 9 s because its high-density effects suppress neutrino opacities.

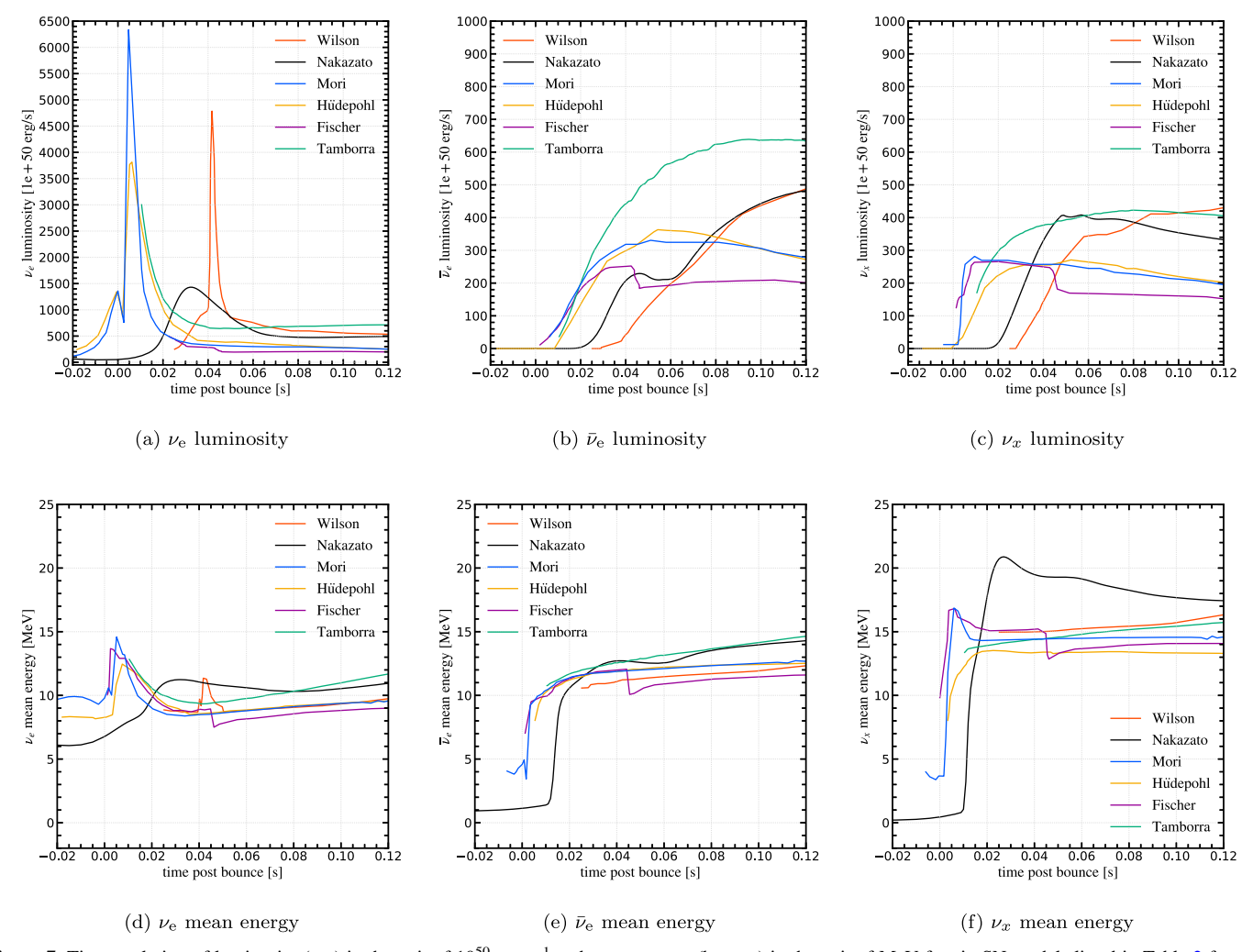


Figure 7. Time evolution of luminosity (top) in the unit of 10^{50} erg s⁻¹ and mean energy (bottom) in the unit of MeV for six SN models listed in Table 2 for each neutrino flavor, from -0.02 to 0.12 s (the core bounce occurs at 0 s). Here, ν_x means any of ν_μ , ν_τ , $\bar{\nu}_\mu$, and $\bar{\nu}_\tau$. The red, black, blue, orange, purple, and green lines represent the Wilson model, the Nakazato model, the Mori model, the Hüdepohl model, the Fischer model, and the Tamborra model, respectively, as indicated by the legend in each panel. The striking peak in (a) for some models corresponds to the neutronization burst, and a dip before the neutronization burst seen in the Mori model and the Hüdepohl model corresponds to neutrino trapping.

4.1.5. The Fischer Model

The Fischer model (Fischer et al. 2010) is a onedimensional SN model including three progenitors: the $8.8\,M_{\odot}$ O-Ne-Mg-core progenitor modeled by Nomoto (1987), which is the same as the one used in the Hüdepohl model, and the 10.8 and $18 M_{\odot}$ Fe-core progenitors in Woosley et al. (2002). This model utilizes AGILE-BOLTZTRAN (Liebendörfer et al. 2004), a spherically symmetric, general relativistic hydrodynamics code (AGILE) with a Boltzmann neutrino transport solver (BOLTZTRAN). It also uses Shen's EoS (Shen et al. 1998, 1998). While the $8.8 M_{\odot}$ progenitor explodes successfully, the 10.8 and $18 M_{\odot}$ progenitors do not explode naturally. In the latter two cases, neutrino reaction rates have been artificially enhanced to produce a successful explosion. In this article we have selected the naturally exploding $8.8 M_{\odot}$ model and use data scanned from Figures 2 and 14 of Fischer et al. (2010), which include emission up to \sim 6 s after the core bounce. Hereafter, "the Fischer model" indicates these data.

4.1.6. The Tamborra Model

The Tamborra model (Tamborra et al. 2014) is a pioneering three-dimensional simulation with energy-dependent neutrino transport. It has three progenitors with different masses (11.2, 20, $27 M_{\odot}$). The simulated time range is up to $\sim 350 \,\mathrm{ms}$ for the 11.2 and 20 M_{\odot} progenitor cases and up to \sim 550 ms for the 27 M_{\odot} progenitor case; however, none of these explodes successfully within these simulation periods. The model uses the neutrinoradiation hydrodynamics code PROMETHEUS-VERTEX and the Lattimer EoS with compressibility $K = 220 \,\text{MeV}$ (Lattimer & Swesty 1991), often referred to as LS EoS. For the 20 and $27 M_{\odot}$ progenitor cases, quasi-periodic oscillations appear in the neutrino signal due to SASI effects (Marek & Janka 2009). Since this signal modulation depends on the angular direction of the observer relative to the progenitor, the model considers three observer directions for each progenitor mass. We use data for the $27 M_{\odot}$ progenitor with the "black" observer direction in Tamborra et al. (2014) provided by the SN simulation pipeline SNEWPY (Baxter et al. 2022). Hereafter, "the Tamborra model" indicates this case.

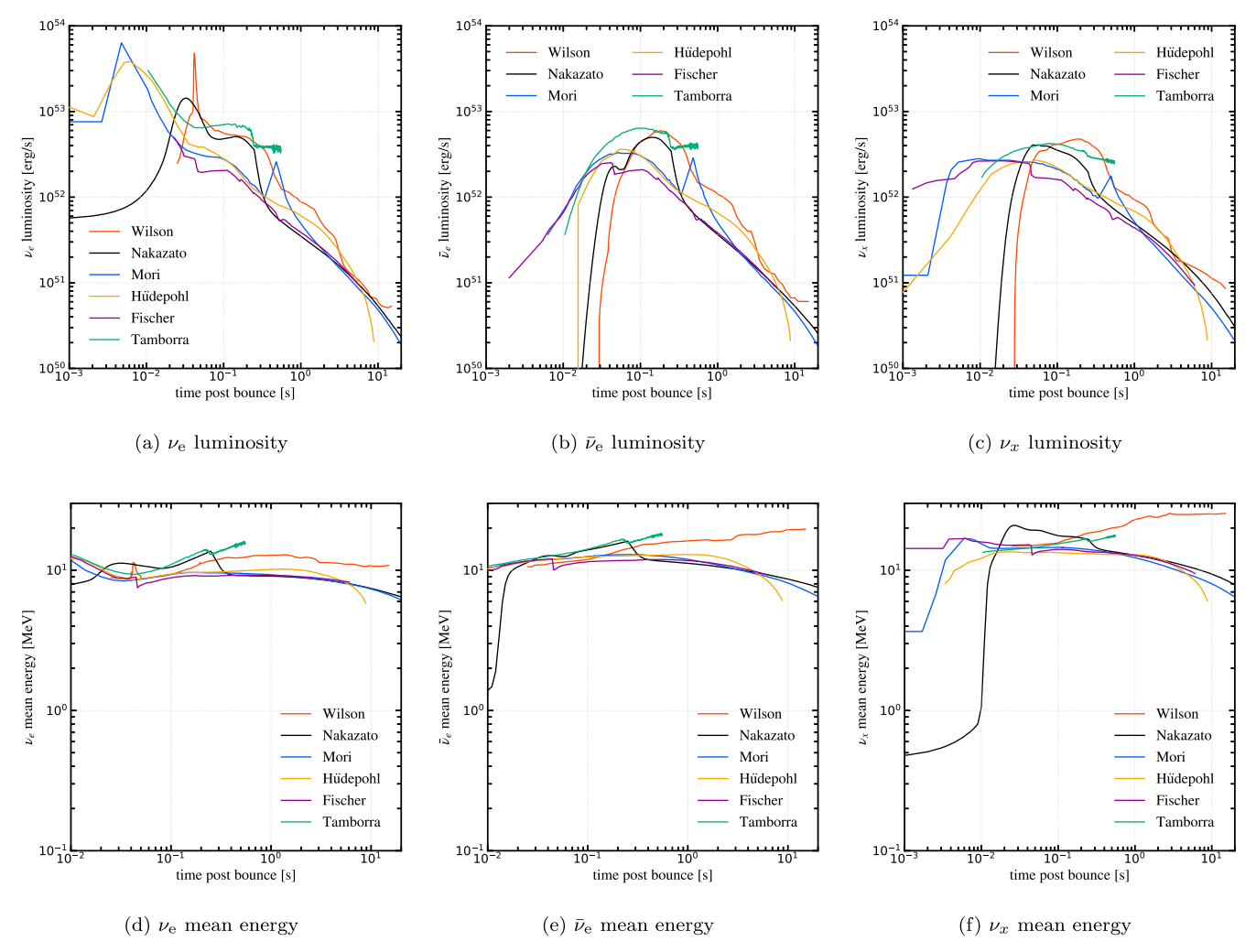


Figure 8. Same as Figure 7 but shows a longer time range up to 20 s (the core bounce occurs at 0 s). Note that luminosity is expressed in logarithmic scale in the unit of erg s.

4.2. Event Generation

We generate events in SK using SKSNSim (Super-Kamiokande Supernova Simulation), an event generator for SN-related neutrino interactions (Nakanishi et al. 2024). As illustrated in Figure 6, for an SN at a given distance in an arbitrarily chosen position and a given neutrino oscillation case, SKSNSim computes the expected number of the neutrino interactions listed in Section 2 and generates events from the fluxes of the input SN model and cross sections. For each interaction r, the expected number of events in each true time and energy bin (E_{ν} , t) is calculated as:

$$\frac{d^2N_r(E_\nu, t)}{dtdE_\nu} = N_r \sigma_r(E_\nu) \frac{d\phi(E_\nu, t)}{dE_\nu}$$
 (10)

where N_r represents the number of targets (protons, electrons, or oxygen nuclei, available to interaction r) in the full inner volume of SK (32.5k m³), $\sigma(E_{\nu})$ is the cross section for interaction r as a function of the neutrino energy, E_{ν} , and $d\phi$ (E_{ν} , t)/ dE_{ν} stands for the neutrino flux. We note that the neutrino flavor in Equation (10) depends on the interaction r. The cross-section calculations are taken from Strumia & Vissani (2003) for IBD, from Bahcall et al. (1995) for ES, from Suzuki et al. (2018) and Nakazato et al. (2018) for 16 O CC

interactions, and from Langanke et al. (1996) and Kolbe et al. (2002) for 16 O NC interactions. The backward anisotropy of the angular distribution in the event topology of the 16 O CC interactions (Tomas et al. 2003) and the isotropic gamma-ray emission from the 16 O NC interaction are considered. By integrating Equation (10) over time and energy, the expected number of events for the interaction r for a single SN explosion is obtained. SKSNSim then generates events using this value as the mean of a Poisson random process for each r.

Three-flavor neutrino oscillations including matter effects inside the SN are considered based on the calculation in Dighe & Smirnov (2000). Assuming the normal mass ordering (NMO), the relationship between the number of neutrinos generated in a collapsing star $N_{\nu_i}^{\rm gen}$ and the number of neutrinos at the stellar surface $N_{\nu_i}^{\rm sur}$ for each flavor $i=e,\,\mu,\,\tau$ is given by

$$N_{\nu_e}^{\text{sur}} = N_{\nu_r}^{\text{gen}} \tag{11}$$

$$N_{\nu_{\rm r}}^{\rm sur} = N_{\nu_{\rm r}}^{\rm gen} + N_{\nu_{\rm r}}^{\rm gen} \tag{12}$$

$$N_{\bar{\nu}_e}^{\text{sur}} = N_{\bar{\nu}_e}^{\text{gen}} \times \cos^2 \theta_{12} + N_{\bar{\nu}_r}^{\text{gen}} \times \sin^2 \theta_{12}$$
 (13)

$$N_{\bar{\nu}_x}^{\text{sur}} = N_{\bar{\nu}_e}^{\text{gen}} \times \sin^2 \theta_{12} + N_{\bar{\nu}_x}^{\text{gen}} \times (1 + \cos^2 \theta_{12}),$$
 (14)

Table 3

Average Number of Events at SK Generated by SKSNSim

Generated by	Wilson			Nakazato	Nakazato				
SKSNSim	No Osc.	NMO	IMO	No Osc.	NMO	IMO	No Osc.	NMO	IMO
IBD (ν̄ _e)	7431	8207	9970	3542	3893	4693	3275	3422	3745
ES (ν_e)	223	231	229	173	172	171	177	148	156
ES $(\bar{\nu}_e)$	97	97	98	63	66	72	60	61	63
ES (ν_x)	80	79	80	60	60	60	52	57	56
ES $(\bar{\nu}_x)$	69	69	69	52	51	48	45	45	44
$^{16}{ m O}~{ m CC}~(\nu_{ m e})$	44	1034	729	48	180	139	8	86	62
$^{16}{ m O~CC}~(\bar{\nu}_{\rm e})$	195	329	633	46	68	116	30	42	71
16 O NC ($\nu_{\rm e}$, 15 N)	4	89	63	4	15	12	1	8	5
16 O NC ($\bar{\nu}_{\rm e}$, 15 N)	22	43	89	5	8	16	3	4	8
16 O NC $(\nu_x, ^{15}$ N)	177	93	119	31	20	23	15	8	10
16 O NC $(\bar{\nu}_{x},^{15}$ N)	177	156	112	31	28	21	15	14	10
16 O NC ($\nu_{\rm e}$, 15 O)	1	24	17	1	4	3	0	2	1
16 O NC ($\bar{\nu}_{\rm e}$, 15 O)	6	12	24	1	2	4	1	1	2
16 O NC $(\nu_x, ^{15}$ O)	48	25	32	9	5	6	4	2	3
¹⁶ O NC ($\bar{\nu}_{x}$, ¹⁵ O)	48	42	30	8	8	5	4	4	3
Total	8622	10,530	12,294	4074	4580	5389	3690	3904	4239
Generated by	Hüdepohl			Fischer			Tamborra		
SKSNSim	No Osc.	NMO	IMO	No Osc.	NMO	IMO	No Osc.	NMO	IMO
IBD ($\bar{\nu}_e$)	3048	3052	3049	1884	1990	2242	3830	3487	2718

SKSNSim	Hudeponi			Fischer			татноотта			
	No Osc.	NMO	IMO	No Osc.	NMO	IMO	No Osc.	NMO	IMO	
$\overline{\text{IBD }(\bar{\nu}_{e})}$	3048	3052	3049	1884	1990	2242	3830	3487	2718	
ES (ν_e)	146	124	132	90	87	88	135	82	99	
ES $(\bar{\nu}_e)$	53	53	53	35	35	37	50	45	35	
ES (ν_x)	43	47	46	31	31	31	28	38	35	
ES $(\bar{\nu}_x)$	38	38	38	27	26	25	25	26	30	
16 O CC ($\nu_{\rm e}$)	12	32	26	5	27	21	55	90	80	
$^{16}{ m O~CC}~(\bar{\nu}_{\rm e})$	30	31	33	15	18	27	97	90	77	
16 O NC ($\nu_{\rm e}$, 15 N)	1	3	2	0	2	2	5	8	7	
16 O NC ($\bar{\nu}_{\rm e}$, 15 N)	3	3	3	1	2	2	11	10	8	
16 O NC $(\nu_x, ^{15}$ N)	6	4	4	5	3	4	16	13	14	
16 O NC $(\bar{\nu}_x, ^{15}$ N)	6	6	6	5	4	4	16	17	19	
16 O NC ($\nu_{\rm e}$, 15 O)	0	1	1	0	1	1	1	2	2	
16 O NC ($\bar{\nu}_{\rm e}$, 15 O)	1	1	1	0	0	1	3	3	2	
16 O NC $(\nu_x, ^{15}$ O)	1	1	1	1	1	1	4	3	4	
16 O NC ($\bar{\nu}_{x}$, 15 O)	2	2	1	1	1	1	4	5	5	
Total	3390	3398	3396	2100	2228	2487	4280	3919	3135	

Note. Note that ν_x represents ν_μ and ν_τ . No energy cut is applied.

where $N_{\nu_x}^{\text{gen}}$ represents $N_{\nu_\mu}^{\text{gen}}$ or $N_{\nu_\tau}^{\text{gen}}$, while $N_{\nu_x}^{\text{sur}} = N_{\nu_\mu}^{\text{sur}} + N_{\nu_\tau}^{\text{sur}}$. For the inverted mass ordering (IMO) the relations are

$$N_{\nu_e}^{\text{sur}} = N_{\nu_e}^{\text{gen}} \times \sin^2 \theta_{12} + N_{\nu_r}^{\text{gen}} \times \cos^2 \theta_{12}$$
 (15)

$$N_{\nu_x}^{\text{sur}} = N_{\nu_e}^{\text{gen}} \times \cos^2 \theta_{12} + N_{\nu_x}^{\text{gen}} \times (1 + \sin^2 \theta_{12})$$
 (16)

$$N_{\bar{\nu}_{\rm e}}^{\rm sur} = N_{\bar{\nu}_{\rm r}}^{\rm gen} \tag{17}$$

$$N_{\bar{\nu}_{r}}^{\text{sur}} = N_{\bar{\nu}_{r}}^{\text{gen}} + N_{\bar{\nu}_{r}}^{\text{gen}}.$$
 (18)

Note that matter effects within the earth are not considered in SKSNSim.

SKSNSim was initially developed to read flux data from the Nakazato model's data format (denoted "Nakazato format" hereafter), which provides the differential neutrino flux and the differential neutrino luminosity at each time *t* for each neutrino flavor in bins of energy. To process other SN models with different data formats, we converted each to "Nakazato format" (data format unification) as presented in Appendix A.

4.3. Detector Simulation

Events generated with SKSNSim are next processed with SKG4 (Super-Kamiokande GEANT4-based simulation) and mccomb_sn (Monte Carlo Combine for Supernova) as illustrated in Figure 6. SKG4 (Harada 2020) includes Cherenkov radiation, photon scattering, absorption, and reflection in the water (or Gd solution) as well as similar processes on other detector materials. Further it simulates the response of the SK PMTs to photons and the subsequent response of their readout electronics. In this work SKG4 adopts GEANT4 version 4.10.05.p01 with several modifications. In particular, the model of neutron capture on Gd, ANNRI-Gd (Hagiwara et al. 2019; Tanaka et al. 2020), has been implemented for this work. All analyses in this article are performed under the assumption of 0.033% Gd concentration.

After processing with SKG4, the mccomb_sn program is responsible for adding realistic dark noise, building events, and applying the software trigger. Given the complexity of radioactive backgrounds in the SK detector, it is impossible to reliably simulate them with MC models alone. Instead, hits

Table 4
Average Number of Reconstructed Events at SK-Gd

Reconstructed	Wilson			Nakazato			Mori		
	No Osc.	NMO	IMO	No Osc.	NMO	IMO	No Osc.	NMO	IMO
$\overline{\mathrm{IBD}} \; (\bar{\nu}_{\mathrm{e}})$	4879	5364	6465	2221	2434	2921	2048	2144	2355
ES (ν_e)	69	106	95	43	57	53	44	46	45
ES $(\bar{\nu}_e)$	22	25	30	10	11	13	9	9	10
ES (ν_x)	34	28	30	18	16	17	15	14	14
ES $(\bar{\nu}_x)$	28	27	26	15	14	13	12	11	11
$^{16}O\ CC\ (\nu_{\rm e})$	27	660	465	29	108	83	4	56	40
^{16}O CC $(\bar{\nu}_e)$	126	208	394	28	41	69	19	27	45
16 O NC ($\nu_{\rm e}$, 15 N)	0	0	0	0	0	0	0	0	0
16 O NC ($\bar{\nu}_{e}$, 15 N)	0	0	0	0	0	0	0	0	0
16 O NC $(\nu_x, ^{15}$ N)	0	0	0	0	0	0	0	0	0
¹⁶ O NC $(\bar{\nu}_x, ^{15}N)$	0	0	0	0	0	0	0	0	0
16 O NC $(\nu_e, ^{15}$ O)	0	0	0	0	0	0	0	0	0
16 O NC ($\bar{\nu}_{\rm e}$, 15 O)	0	0	0	0	0	0	0	0	0
16 O NC $(\nu_x, ^{15}$ O)	0	0	0	0	0	0	0	0	0
¹⁶ O NC $(\bar{\nu}_x,^{15}O)$	0	0	0	0	0	0	0	0	0
Total	5185	6418	7505	2364	2681	3169	2151	2307	2520

Reconstructed	Reconstructed	Hüdepohl		Fischer			Fischer Tamb			
	No Osc.	NMO	IMO	No Osc.	NMO	IMO	No Osc.	NMO	IMO	
IBD ($\bar{\nu}_{\rm e}$)	1936	1939	1935	1186	1260	1437	2505	2283	1786	
ES (ν_e)	38	39	39	22	29	26	46	33	37	
ES $(\bar{\nu}_e)$	9	8	8	5	6	6	12	10	8	
ES (ν_x)	12	12	12	9	8	8	10	12	12	
$\mathrm{ES}(\bar{\nu}_{x})$	10	10	10	7	7	7	8	9	10	
16 O CC ($\nu_{\rm e}$)	7	19	16	3	17	13	35	58	51	
^{16}O CC $(\bar{\nu}_{\rm e})$	19	20	21	9	11	17	62	58	49	
16 O NC ($\nu_{\rm e}$, 15 N)	0	0	0	0	0	0	0	0	0	
16 O NC ($\bar{\nu}_{\rm e}$, 15 N)	0	0	0	0	0	0	0	0	0	
16 O NC $(\nu_x, ^{15}$ N)	0	0	0	0	0	0	0	0	0	
16 O NC $(\bar{\nu}_{x},^{15}N)$	0	0	0	0	0	0	0	0	0	
16 O NC ($\nu_{\rm e}$, 15 O)	0	0	0	0	0	0	0	0	0	
16 O NC ($\bar{\nu}_{\rm e}$, 15 O)	0	0	0	0	0	0	0	0	0	
16 O NC $(\nu_x, ^{15}$ O)	0	0	0	0	0	0	0	0	0	
16 O NC $(\bar{\nu}_{x}, ^{15}$ O)	0	0	0	0	0	0	0	0	0	
Total	2031	2037	2041	1241	1338	1514	2678	2463	1953	

Note. Here, the phrase "reconstructed events" means the events reconstructed in SNWATCH from the PMT signal of the SKSNSim-generated events, and the IBD tagging is not applied to them yet. The events with energy 7 MeV or more are selected as "prompt" candidates (see Section 3.1 for details). With this 7 MeV energy cut, the number of reconstructed ¹⁶O NC events is zero. As the original information generated by SKSNSim is lost during the mccomb_sn process, to identify the interaction of the reconstructed event, the reconstructed events are associated with the SKSNSim-generated event; the condition of less than 0.02 μ s time difference between the SKSNSim-generated event and the closest reconstructed event is applied. Note that ν_x represents ν_μ and ν_τ .

from randomly triggered data 1 ms in length in the actual detector are added to the simulated events. Since most of these hits are generated by backgrounds, this creates a realistic simulation of how SN burst events would appear in SK. In the next step, sequences of simulated events are altered to have the same time structure as expected during a real neutrino burst. Ideally, each neutrino interaction would represent a single event in the detector. However, multiple neutrino interactions can occur within the standard SK DAQ timing block of $17 \mu s$ (Nishino et al. 2007; Orii et al. 2014; Orii 2015) and further hits from neighboring interactions may overlap in time with one another. To simulate this, events are assigned random times consistent with their expected event rate evolution, and all hits from all events are then laid out in time. These are then separated into 17 μ s blocks, as is done with the real data, and the software trigger is applied. Based on the triggers raised, the hits are repackaged into events using hits before and after the

trigger condition was met. For this reason, all hits in the final event may not necessarily have a one-to-one correspondence with those from the initial interaction that created them; they may be associated with a neighboring event via this process.

5. Simulated Interaction Events in SK-Gd and Their Detector Responses

In the following, we discuss simulated interactions in SK-Gd and the response of the detector assuming an SN burst located at 10 kpc for each of the six models as described in Section 4. For each model, three types of neutrino oscillation scenarios are studied: without oscillation (No Osc.) and neutrino oscillations under NMO and IMO. The calculation assumes $\sin^2\theta_{12} = 0.307$ (Particle Data Group et al. 2022). As mentioned in Section 3.3, though SNWATCH typically uses 3000 MC trials to determine the pointing accuracy to an SN,

Table 5
The IBD-tagging Performance for the Six SN Models for an SN Burst Located at 10 kpc in the NMO Scenario

Wilson	True IBD	True ES	True ¹⁶ O CC	True ¹⁶ O NC	True Gd-n	Other
Efficiency (%)	48.48 ± 0.03	0.0 ± 0.02	8.8 ± 0.03	0.0 ± 0.01	0.0 ± 0.01	
IBD-like purity (%)	97.97 ± 0.01	0.0 ± 0.01	2.2 ± 0.01	0.0 ± 0.01	0.0 ± 0.01	0.0 ± 0.01
ES-like purity (%)	69.69 ± 0.03	4.4 ± 0.02	21.21 ± 0.03	0.0 ± 0.01	4.4 ± 0.02	0.0 ± 0.01
Nakazato	True IBD	True ES	True ¹⁶ O CC	True ¹⁶ O NC	True Gd-n	Other
Efficiency (%)	46.46 ± 0.04	0.0 ± 0.02	8.8 ± 0.08	0.0 ± 0.02	0.0 ± 0.01	
IBD-like purity (%)	98.98 ± 0.01	0.0 ± 0.01	1.1 ± 0.01	0.0 ± 0.01	0.0 ± 0.01	0.0 ± 0.01
ES-like purity (%)	78.78 ± 0.04	6.6 ± 0.03	9.9 ± 0.03	0.0 ± 0.01	5.5 ± 0.02	0.0 ± 0.01
Mori	True IBD	True ES	True ¹⁶ O CC	True ¹⁶ O NC	True Gd-n	Other
Efficiency (%)	47.47 ± 0.04	0.0 ± 0.02	8.8 ± 0.1	0.0 ± 0.03	0.0 ± 0.01	
IBD-like purity (%)	99.99 ± 0.01	0.0 ± 0.01	0.0 ± 0.01	0.0 ± 0.01	0.0 ± 0.01	0.0 ± 0.01
ES-like purity (%)	81.81 ± 0.04	6.6 ± 0.03	5.5 ± 0.03	0.0 ± 0.01	5.5 ± 0.03	0.0 ± 0.01
Hüdepohl	True IBD	True ES	True ¹⁶ O CC	True ¹⁶ O NC	True Gd-n	Other
Efficiency (%)	47.47 ± 0.04	0.0 ± 0.02	11.11 ± 0.16	0.0 ± 0.04	0.0 ± 0.01	
IBD-like purity (%)	99.99 ± 0.01	0.0 ± 0.01	0.0 ± 0.01	0.0 ± 0.01	0.0 ± 0.01	0.0 ± 0.01
ES-like purity (%)	84.84 ± 0.04	6.6 ± 0.03	3.3 ± 0.02	0.0 ± 0.01	5.5 ± 0.03	0.0 ± 0.01
Fischer	True IBD	True ES	True ¹⁶ O CC	True ¹⁶ O NC	True Gd-n	Other
Efficiency (%)	47.47 ± 0.05	0.0 ± 0.02	9.9 ± 0.17	0.0 ± 0.06	0.0 ± 0.01	•••
IBD-like purity (%)	99.99 ± 0.01	0.0 ± 0.01	0.0 ± 0.01	0.0 ± 0.01	0.0 ± 0.01	0.0 ± 0.01
ES-like purity (%)	83.83 ± 0.05	6.6 ± 0.03	3.3 ± 0.03	0.0 ± 0.01	5.5 ± 0.03	0.0 ± 0.01
Tamborra	True IBD	True ES	True ¹⁶ O CC	True ¹⁶ O NC	True Gd-n	Other
Efficiency (%)	48.48 ± 0.04	0.0 ± 0.03	14.14 ± 0.1	0.0 ± 0.02	0.0 ± 0.01	
IBD-like purity (%)	98.98 ± 0.02	0.0 ± 0.01	1.1 ± 0.02	0.0 ± 0.01	0.0 ± 0.01	0.0 ± 0.01
ES-like purity (%)	82.82 ± 0.04	4.4 ± 0.02	7.7 ± 0.03	0.0 ± 0.01	5.5 ± 0.02	0.0 ± 0.01

Note. IBD-like selection efficiency (Equation (19)), IBD-like purity (Equation (20)), and ES-like purity (Equation (21)) are shown in units of percent. The errors are the statistical uncertainty of Monte Carlo samples.

due to limited computing resources for this study, 1000 MC trials are used here for each combination of SN model and oscillation scenario. We note that all simulations use a common SN position, arbitrarily chosen to be the position of the Sun at 0:00 on 23 March 2011 (i.e., R.A. = $1^h41^m43^s.6$, decl. = $+0^\circ39'12''.5$).

Table 3 shows the average number of events taken from 1000 MC trials of each SN model with events in each trial generated in the full 32.5k m³ of the ID. The number of oxygen-interaction events in Table 3 shows significant differences among models which is also shown in Section 5.2. These differences originate from the energy spectra of incoming neutrinos; since the inelastic interaction cross section is larger at higher neutrino energies (see Figure 2), the detected number of oxygen interactions depends on the neutrino energy.

Table 4 shows the average number of events for each interaction reconstructed in SK-Gd's 22.5k m³ fiducial volume. Note that the original interaction information generated by SKSNSim is lost during the mccomb_sn process as explained in Section 4.3. Therefore, the interaction type that created each reconstructed event is estimated by matching the time of the reconstruction to the time generated by SKSNSim. The closest MC event within $0.02\,\mu s$ of the reconstructed time is considered the parent. Although the fiducial volume is about 70% of the full volume of the detector, more than half of ES events are lost during the event selection process. Low-energy ES events and ^{16}O NC events are removed mainly by the 7 MeV cut in the "prompt" candidate selection.

5.1. SK-Gd's Response with the Nakazato Model

This section presents SK-Gd's response to an SN burst located at 10 kpc simulated with the Nakazato model $(20M_{\odot}, Z=0.02)$ assuming the NMO scenario as a representative example. Similar studies and figures for other models under the IMO scenario are presented in Appendix B. Reconstructed events in the following figures correspond to events after reconstruction in SNWATCH in Figure 3 and after the time matching between the reconstructed time and the generated time by SKSNSim described in Section 5.

Figure 9 shows the time evolution of each interaction across different time ranges, and Figure 10 shows the corresponding time-integrated energy spectra. Most events are concentrated in the first second, as is expected from the luminosity evolution (Figure 8), and IBD events dominate. In Figure 10, energy indicates the reconstructed energy of each mode's visible particles: e⁺ for IBD events, e⁻ for ES, e⁺ or e⁻ for ¹⁶O CC, and gamma-rays from ¹⁶O NC events. These energy spectra are similar in shape over the considered time ranges. The three panels in Figure 11 describe the time-integrated angular distribution of the reconstructed events that satisfy the same criteria described in Section 3.1. Figure 11(a) shows the angular distribution for each interaction. Here, θ_{SN} represents the angle between the true SN direction and the reconstructed direction of the visible particle in each interaction. The shape of the $\cos \theta_{\rm SN}$ distribution reflects the event topology assumed in SKSNSim as mentioned in Section 4.2. The distribution of IBD events (red) has an almost flat but slightly forward

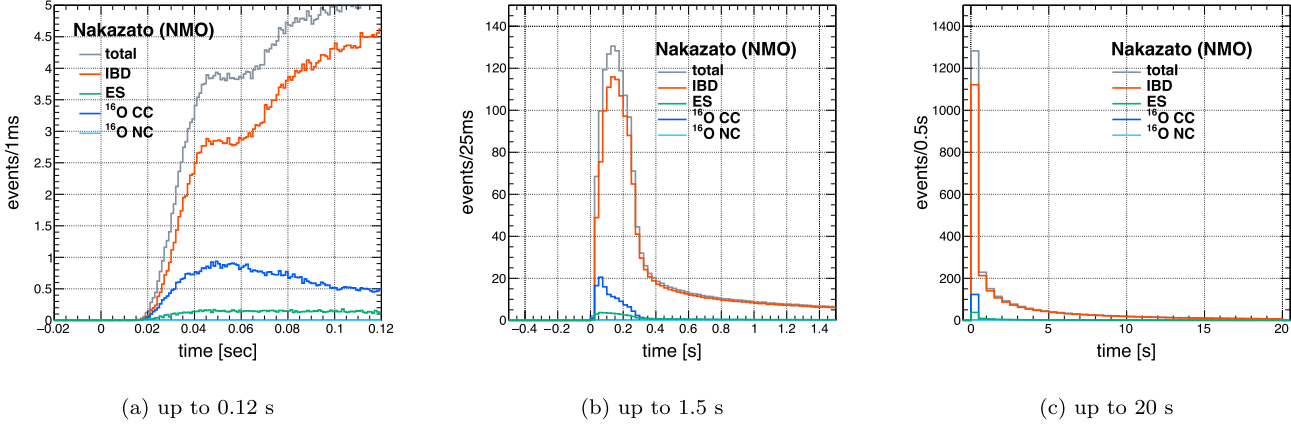


Figure 9. Time evolution of each interaction for the Nakazato model for an SN burst located at 10 kpc with neutrino oscillation in NMO. (a) Up to 0.12 s, (b) up to 1.5 s, and (c) up to 20 s. The red, green, blue, and light-blue histograms represent IBD events, ES events, ¹⁶O CC events, and ¹⁶O NC events, respectively. The gray histogram includes all the interactions.

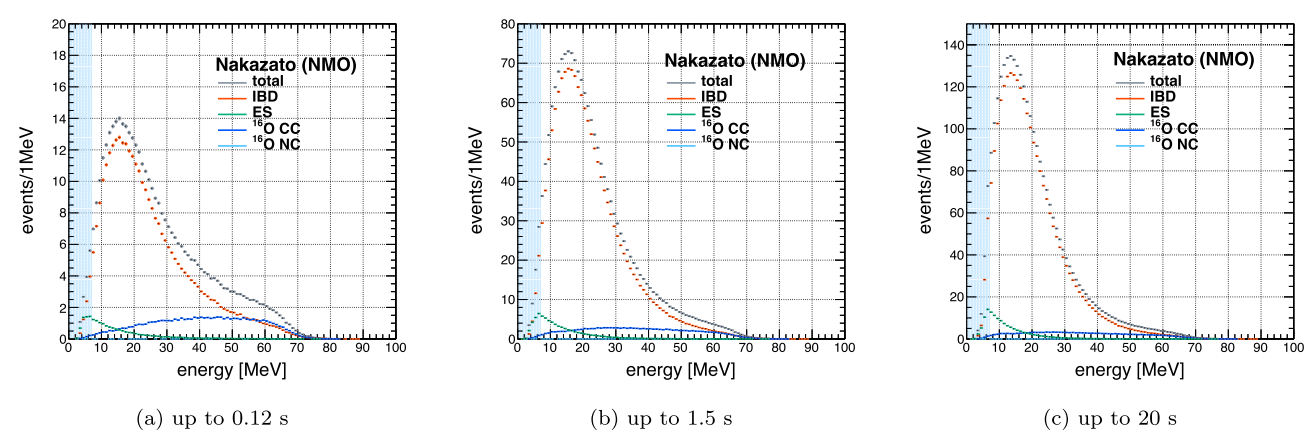


Figure 10. The time-integrated energy spectra of each interaction for the Nakazato model for an SN burst located at 10 kpc with neutrino oscillation in NMO, in the different time ranges: (a) up to 0.12 s, (b) up to 1.5 s, and (c) up to 20 s. Here, the energy indicates the reconstructed energy of e^+ for IBD, e^- for ES, e^+ and e^- for 16 O CC, and the gamma-rays for 16 O NC events. The energy region below the 7 MeV threshold for selecting "prompt" candidates is shaded in light blue.

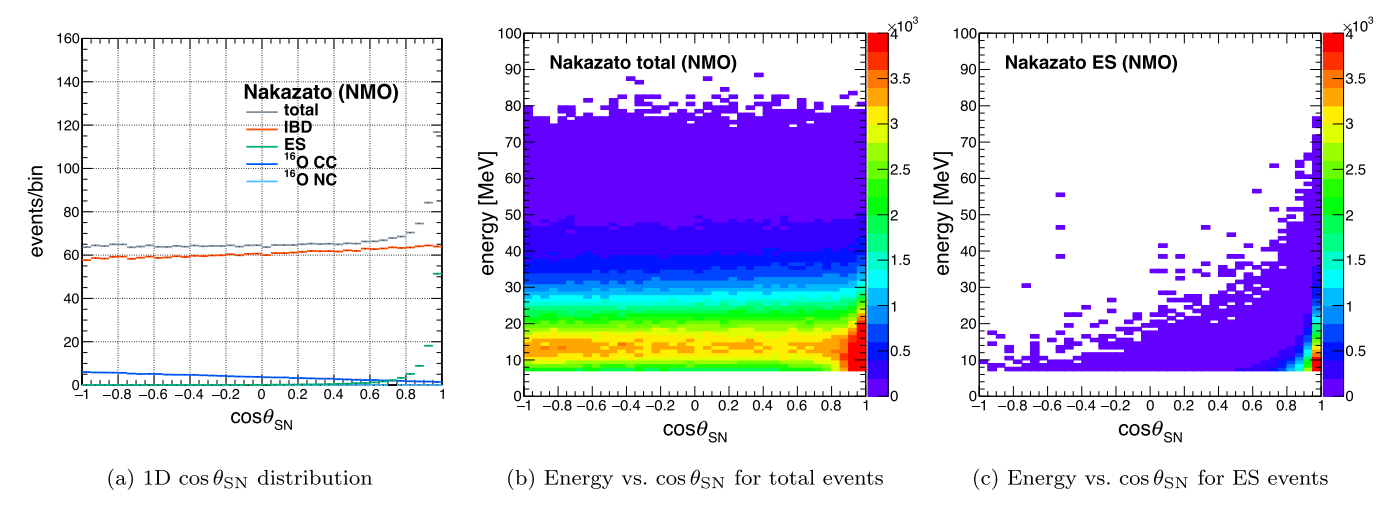


Figure 11. Angular distribution of events for the Nakazato model for an SN burst located at 10 kpc with neutrino oscillation in NMO. (a) 1D $\cos\theta_{\rm SN}$ distribution. The red, green, blue, and light-blue histograms represent IBD events, ES events, $^{16}{\rm O}$ CC events, and $^{16}{\rm O}$ NC events, respectively. The gray histogram includes all the interactions. (b) Energy vs. $\cos\theta_{\rm SN}$ for total events. (c) Energy vs. $\cos\theta_{\rm SN}$ for ES events.

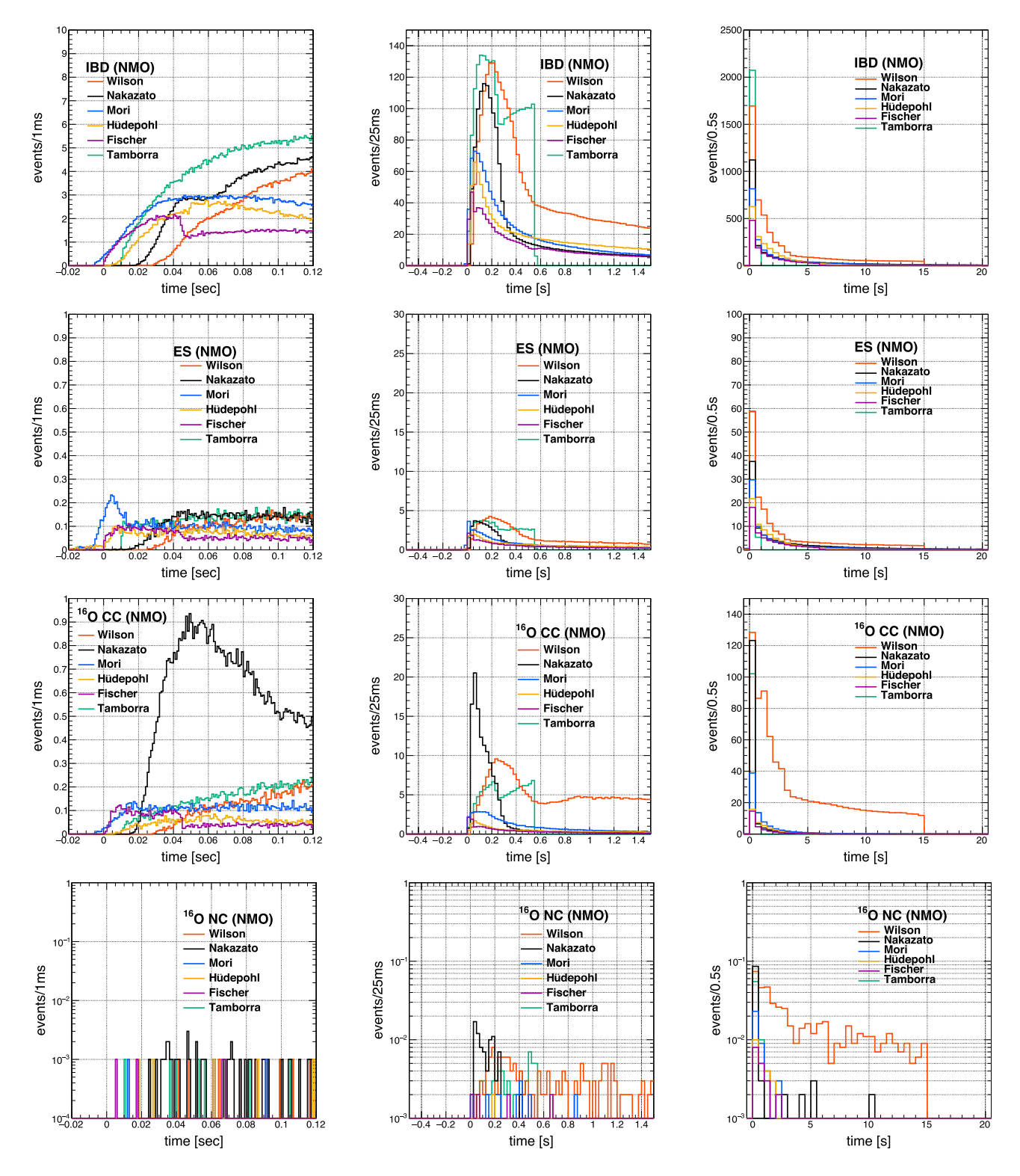


Figure 12. Comparison of time evolution among models for each interaction for an SN burst located at 10 kpc with neutrino oscillation in NMO. The left, middle, and right columns show the time evolution up to 0.12 s, 1.5 s, and 20 s, respectively. Each row represents IBD, ES, ¹⁶O CC, and ¹⁶O NC from top to bottom.

inclination due to positrons being slightly more likely to be emitted in the forward direction at higher neutrino energies. ES (green) events are the result of a forward-scattering process, so the distribution peaks at $\cos\theta_{\rm SN}\sim 1$. On the other hand, $^{16}{\rm O~CC}$ events have a backward bias and, while the

distribution for ¹⁶O NC should be flat, the number of events is too small for it to be observed here.

Figures 11(b) and (c) show $\cos \theta_{\rm SN}$ versus energy distribution for all events and for only ES events, respectively. One might think that using only the high-energy component of ES

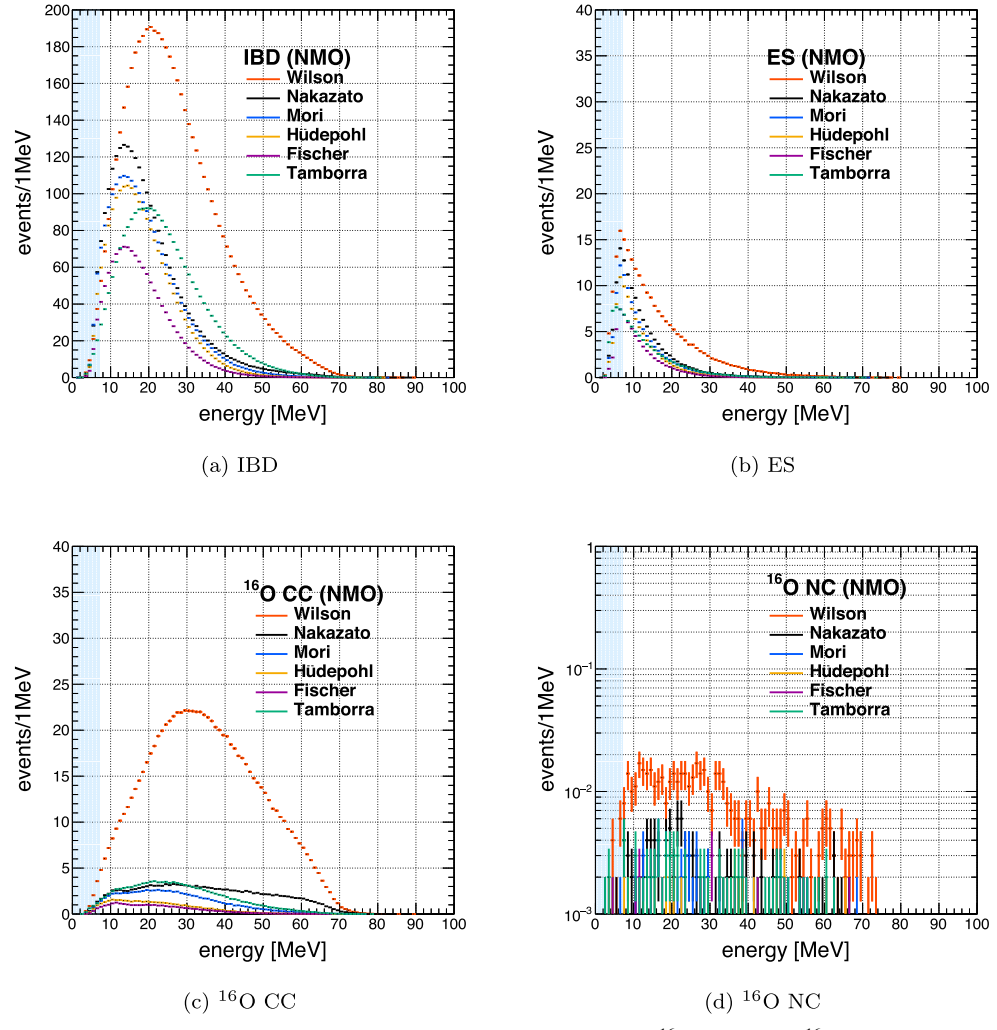


Figure 13. Comparison of energy spectra among models for each interaction: (a) IBD, (b) ES, (c) ¹⁶O CC, and (d) ¹⁶O NC. The energy region below the 7 MeV threshold for selecting "prompt" candidates is shaded in light blue.

events would be effective in determining the direction to the SN because those scattered electrons populate the region $\cos\theta_{\rm SN}\sim 1$. However, as Figure 11(c) suggests, the number of high-energy ES events is insufficient to make a significant contribution to the direction estimation.

5.2. Comparison among Models

This section reports the differences in SK-Gd's response to an SN burst located at 10 kpc, comparing the six SN models described in Section 4.1 and focusing on the NMO oscillation scenario. Appendix B presents corresponding figures for the IMO scenario.

Figure 12 compares the time evolution of reconstructed events among models for each interaction type over three different time ranges. IBD events in the Tamborra model have an increasing feature after the first peak in the event rate, as shown in the top middle of Figure 12, corresponding to Figure 8(b). In the right panel of the second row, the ES peak from the neutronization burst appears in the first 0.1 s for the Mori model (blue). The same feature is seen at around ~ 0.04 s in the Wilson model (red) but is unclear in the other models. To determine whether or not the timing of the neutronization burst can be seen in SK-Gd, we consider the optimistic scenario

given by the Mori model. Note that the excess of ES events over the flat component corresponds to $N_{\nu_e}^{\rm sur}$ in Equations (11)–(12). Integrating from 0.04 to 0.12 s yields the flat component, 93.8 events per second, or 1.4 events expected from -0.002 to 0.017 s. This can be subtracted from the peak component, 4.31 events, obtained by integrating over the same time region, to yield 2.9 events. From the low number of events, it is clear that it would be difficult to observe this difference with any significance for an SN burst located at $10 \, \rm kpc$.

Figure 13 shows a comparison of energy spectra among models considering neutrino oscillation in NMO. The Wilson model and the Tamborra model have higher-energy neutrinos than the other models. As seen in panel (c), the energy spectra of the ¹⁶O CC interaction have significant differences among models, resulting in a large variation in the number of interactions on oxygen in Table 4. Note that ¹⁶O NC interaction events shown in panel (d) are low in energy and small in number as presented in Table 4.

Figure 14 shows comparison of angular distribution of events among models. We note that the general shape of the $\cos\theta_{\rm SN}$ distribution does not depend on the model choice. However, the slope of the $\cos\theta_{\rm SN}$ distribution for IBD and $^{16}{\rm O}$ CC events is steeper in the models with higher mean energy.

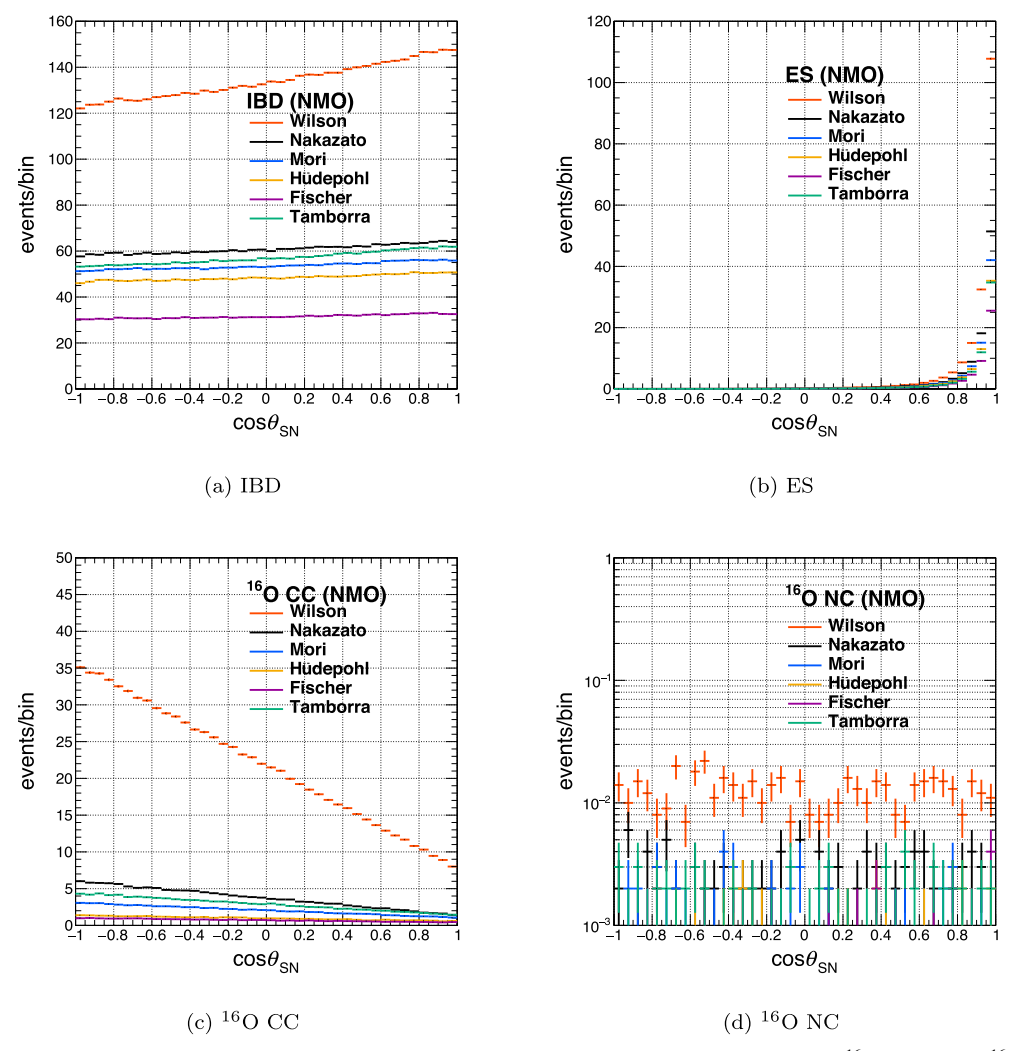


Figure 14. Comparison of $\cos \theta_{SN}$ distribution among models for each interaction: (a) IBD, (b) ES, (c) ^{16}O CC, and (d) ^{16}O NC.

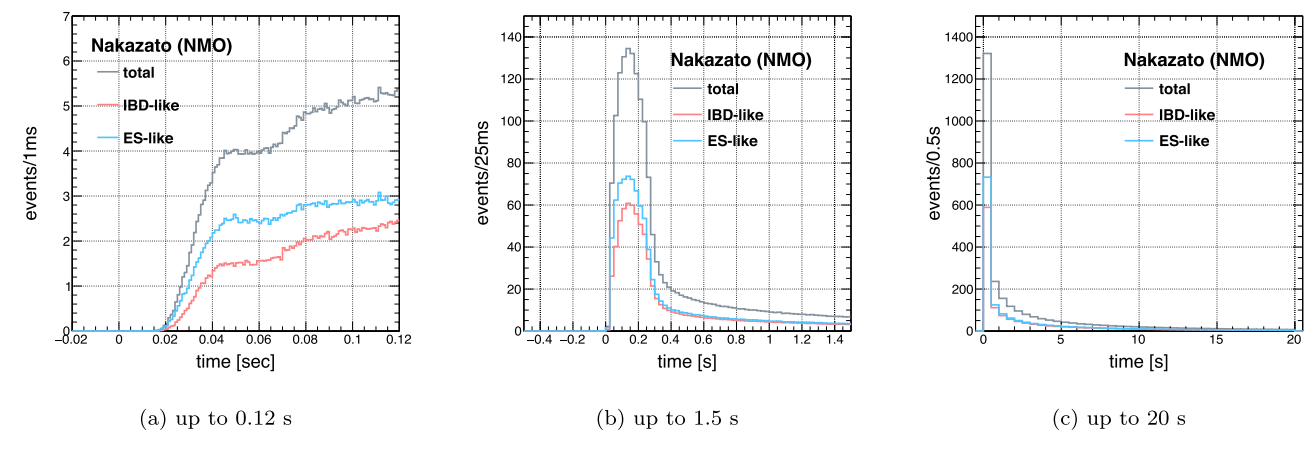


Figure 15. Time evolution of the IBD-like (pink) and ES-like (light blue) events for the Nakazato model for an SN burst located at 10 kpc with neutrino oscillation in NMO. (Same as Figure 9 but for the IBD-like (pink) and ES-like (light blue) events.) (a) Up to 0.12 s, (b) up to 1.5 s, and (c) up to 20 s. The gray histogram is the sum of the pink and light-blue histograms.

6. Performance of IBD Tagging and SN Direction Fit

This section discusses the performance of SNWATCH. In Section 6.1, we report the IBD-tagging performance, focusing

on an SN burst located at 10 kpc assuming the NMO scenario. The SK-Gd's response to events tagged as either IBD-like or otherwise represents the two main event categories that can be observed in SK-Gd. In Section 6.2, we present the pointing

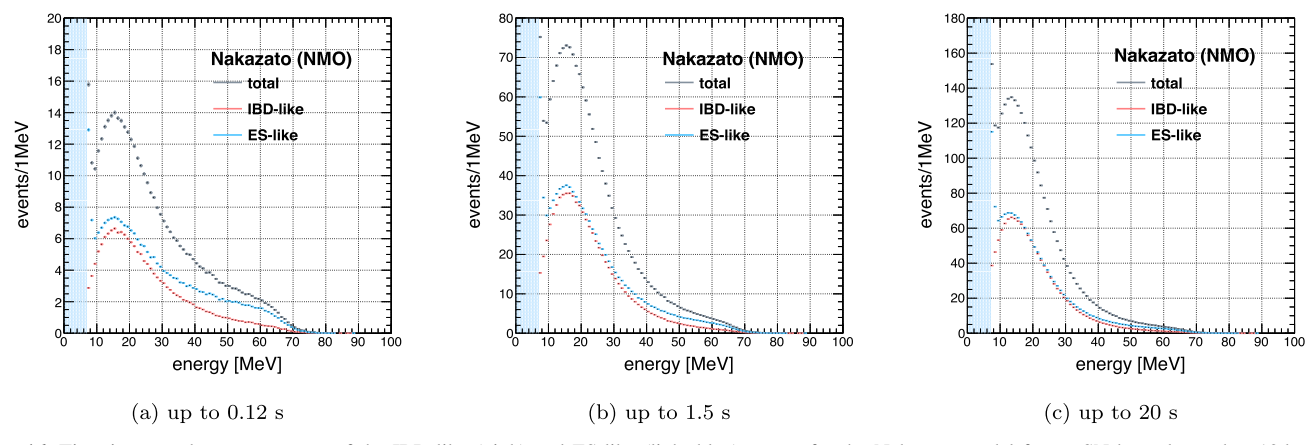


Figure 16. Time-integrated energy spectra of the IBD-like (pink) and ES-like (light blue) events for the Nakazato model for an SN burst located at 10 kpc with neutrino oscillation in NMO in the different time ranges: (a) up to 0.12 s, (b) up to 1.5 s, and (c) up to 20 s. (Same as Figure 10 but for the IBD-like (pink) and ES-like (light blue) events.) Here, the energy indicates the reconstructed energy of e⁺ for IBD, e⁻ for ES, e⁺ and e⁻ for ¹⁶O CC, the gamma-rays for ¹⁶O NC events, the gamma-rays from neutron-capture events, and the other events. The energy region below the 7 MeV threshold for selecting "prompt" candidates is shaded in light blue. The gray histogram is the sum of the pink and light-blue histograms.

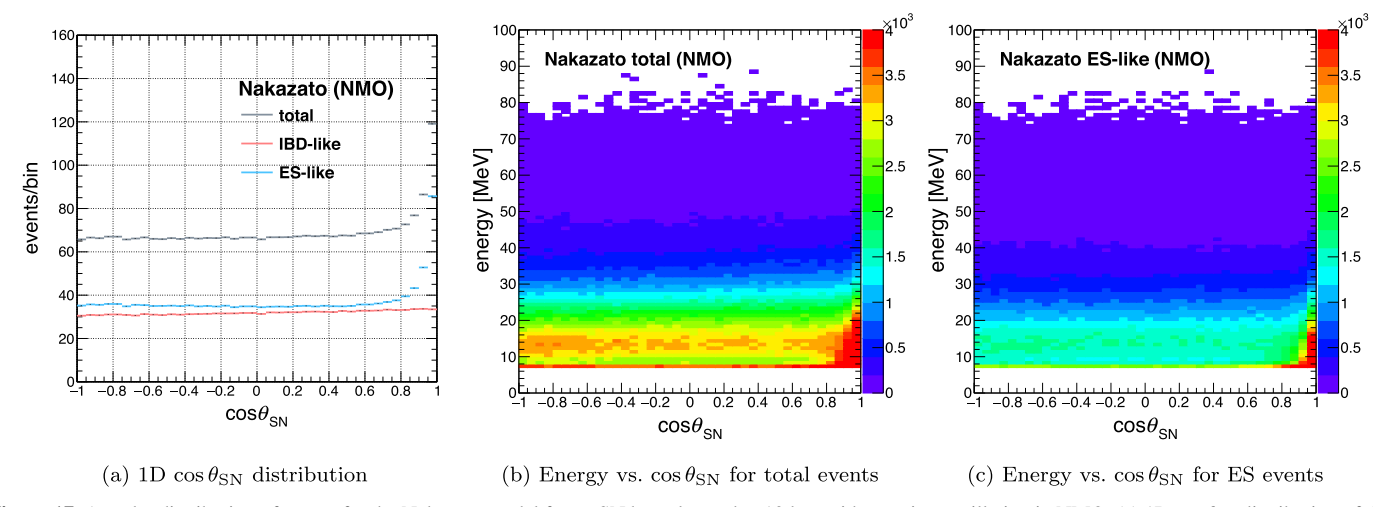


Figure 17. Angular distribution of events for the Nakazato model for an SN burst located at 10 kpc with neutrino oscillation in NMO. (a) 1D $\cos \theta_{SN}$ distribution of the IBD-like (pink) and ES-like (light blue) events. The gray histogram is the sum of the pink and the light-blue histograms. (b) Energy vs. $\cos \theta_{SN}$ for all the reconstructed events. (c) Energy vs. $\cos \theta_{SN}$ for the ES-like events.

accuracy for each SN model assuming an SN burst located at 10 kpc for both NMO and IMO assumptions.

6.1. IBD-tagging Performance

For each interaction X (IBD, ES, ¹⁶O CC, ¹⁶O NC, neutron capture by Gd (Gd-n), or other), the IBD-like selection efficiency, IBD-like purity, and ES-like purity are defined as follows:

$$IBD - like selection efficiency
\equiv \frac{\text{true interaction X tagged as IBD}}{\text{total number of true interaction X}},$$
(19)

$$IBD - like purity$$

$$\equiv \frac{\text{true interaction X tagged as IBD}}{\text{total number of events tagged as IBD}},$$
(20)

ES – like purity
$$\equiv \frac{\text{true interaction X tagged as not IBD}}{\text{total number of events tagged as not IBD}}.$$
(21)

Table 5 shows the efficiency and purity for the six SN models for an SN burst located at 10 kpc in the NMO scenario. We note that the IBD-like selection efficiency for IBD events is about 46%–48% for all six models, but this could potentially be improved by tightening the tagging criterion described in Section 3.1. Further, many true ¹⁶O CC events are mistakenly tagged as IBD-like. We achieved about 97%–99% IBD-like purity for IBD events from all six models. The purity of true IBD events tagged as ES-like varies ~69%–84% depending on the model and is consistently the largest contributor to that sample. However, the true ES component of the ES-like sample still provides pointing to the SN as demonstrated below.

SK-Gd's response after IBD tagging is shown in Figures 15–17 for the Nakazato model assuming the NMO as a

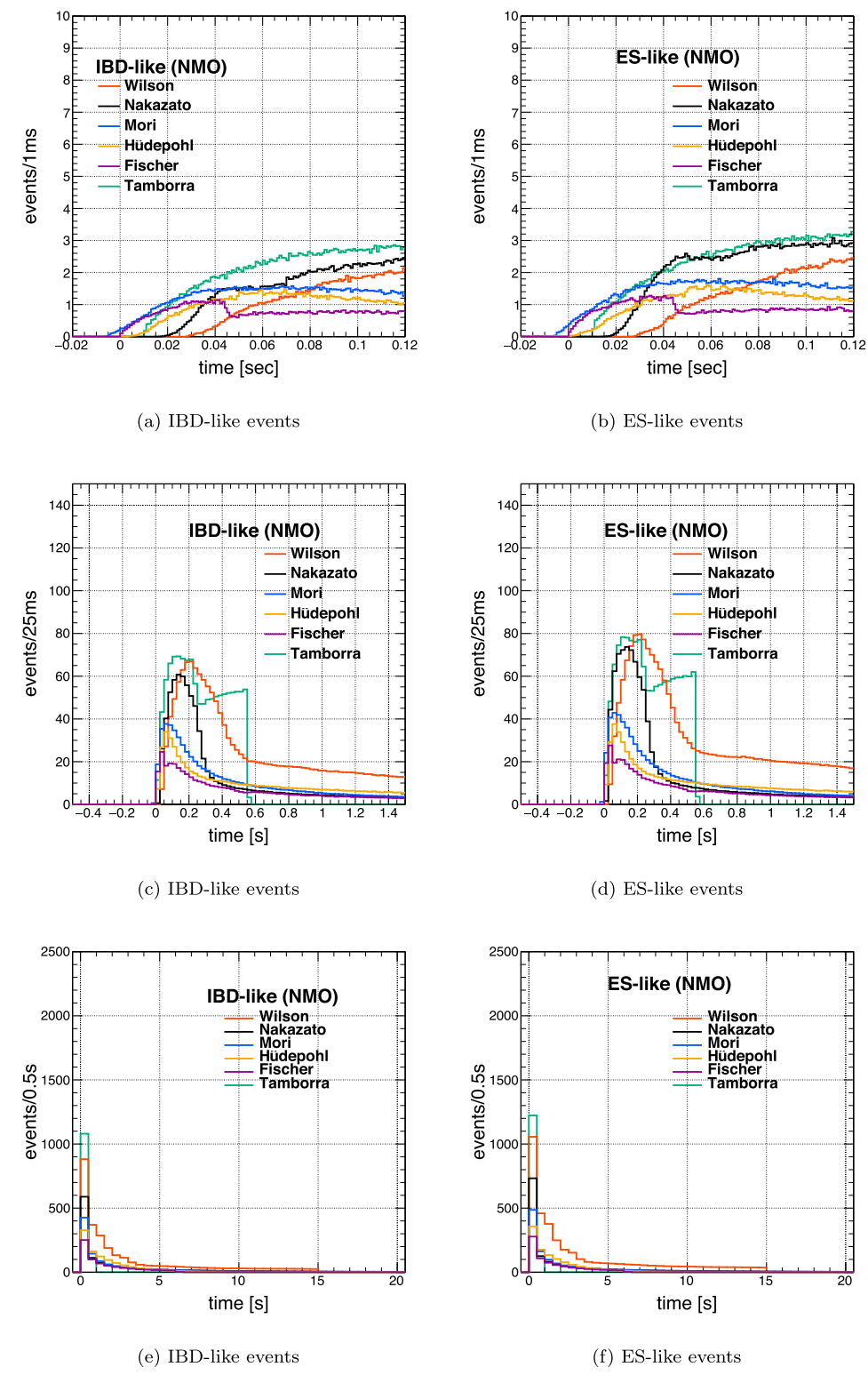


Figure 18. Comparison of time evolution of the IBD-like (left column) and ES-like (right column) events among models for an SN burst located at 10 kpc with neutrino oscillation in the NMO scenario. The top, middle, and bottom rows show the time evolution up to 0.12 s, 1.5 s, and 20 s, respectively.

representative example. Figure 15 shows the time evolution of the IBD-like (pink) and ES-like (light blue) samples. After IBD tagging the time evolution of true ES events and oxygen events is washed out as is shown in Figure 9. The shape of the time evolution of the ES-like events is similar to that of the IBD-like events in Figure 9 for all time ranges due to the large impurity of

true IBD events in the sample. Figure 16 shows the time-integrated energy spectra of the IBD-like (pink) and ES-like (light blue) samples. The peak near 7 MeV in the ES-like sample corresponds to gamma-ray emission from Gd-n capture events. Figure 17(a) shows the angular distribution of the IBD-like (pink) and ES-like (light blue) events. Panels (b) and (c) show two-dimensional plots

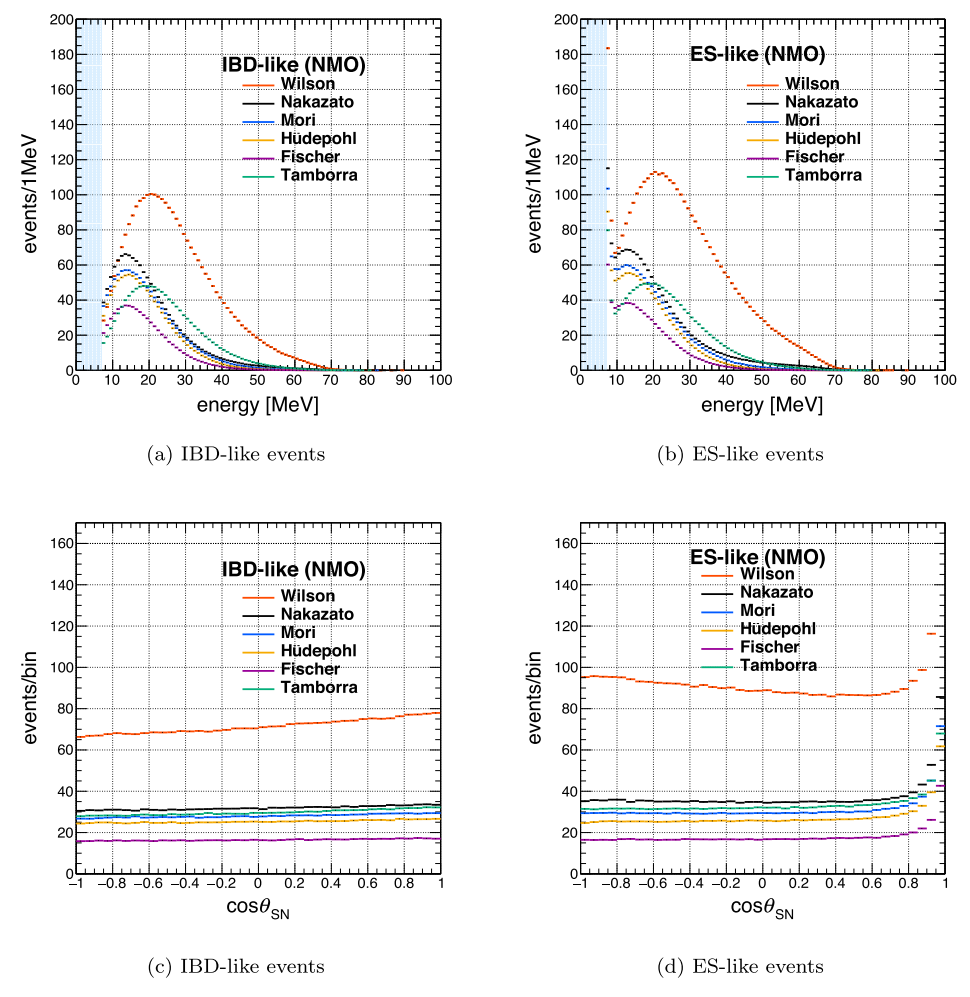


Figure 19. Top: comparison of energy spectra among models for (a) the IBD-like events and (b) the ES-like events. The energy region below the 7 MeV threshold for selecting "prompt" candidates is shaded in light blue. Bottom: comparison of $\cos\theta_{\rm SN}$ distribution among models for (c) the IBD-like events and (d) the ES-like events.

	Wilson			Nakazato			
	No Osc.	NMO	IMO	No Osc.	NMO	IMO	
Pointing accuracy (°)	3.0 ± 0.1	2.5 ± 0.1	2.8 ± 0.1	4.5 ± 0.1	4.0 ± 0.1	4.3 ± 0.1	
	Mori			Hüdepohl			
	No Osc.	NMO	IMO	No Osc.	NMO	IMO	
Pointing accuracy (°)	4.9 ± 0.2	4.6 ± 0.1	4.6 ± 0.1	5.4 ± 0.2	5.1 ± 0.2	5.0 ± 0.2	
	Fischer			Tamborra			
	No Osc.	NMO	IMO	No Osc.	NMO	IMO	
Pointing accuracy (°)	7.2 ± 0.2	6.1 ± 0.2	6.9 ± 0.2	4.6 ± 0.2	5.1 ± 0.2	4.7 ± 0.2	

of the reconstructed energy and $\cos\theta_{\rm SN}$ distributions, respectively. The effect of IBD tagging can be seen by comparing these two panels. Since IBD-like events are removed from (c), there is a stronger peak near $\cos\theta_{\rm SN}\sim 1$ than in (b), which improves the pointing accuracy to the SN.

Similarly the time evolution of the models after sample selection, time-integrated energy, and angular distributions are shown in Figures 18 and 19. The time and energy structures of the events after IBD tagging differ among models.

6.2. Pointing Accuracy for Supernova at 10 kpc

Finally, we derived pointing accuracy for each SN model using the distribution of $\Delta\theta$, where $\cos(\Delta\theta)=\hat{d}_{\rm SN}^{\rm true}\cdot\hat{d}_{\rm SN}^{\rm reco}$

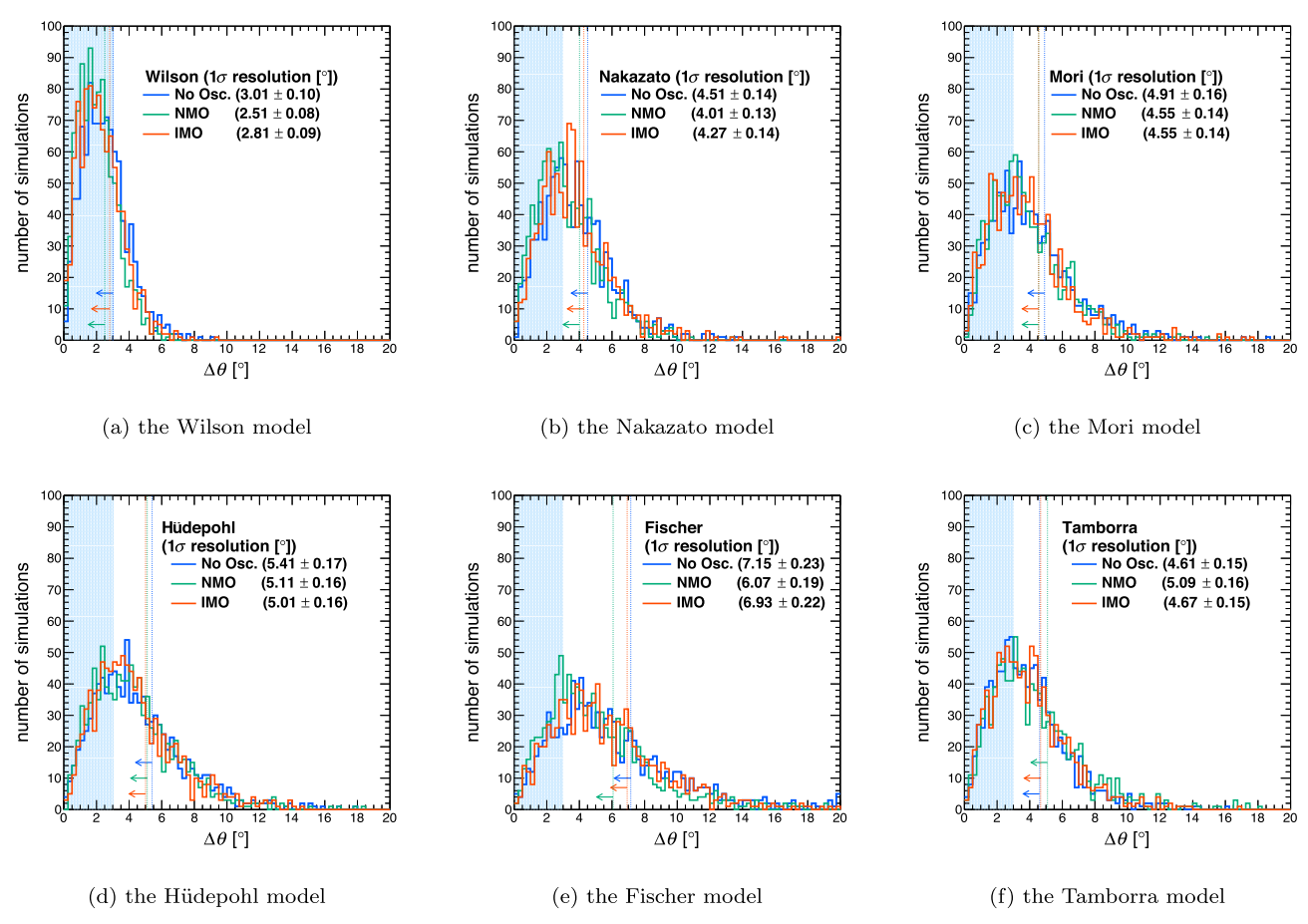


Figure 20. The $\Delta\theta$ distribution of each oscillation scenario for each model for an SN burst located at 10 kpc. The blue, green, and red histograms represent No Osc., NMO, and IMO, respectively. The dashed line and the arrow in each histogram of the corresponding color indicate the pointing accuracy at 1σ , i.e., the value of $\Delta\theta$ up to which the integral of the histogram covers 68% of the 1000 simulations (see Section 3.3). The pointing accuracy for each oscillation assumption in units of degree is also shown in the legend. The shaded region (light blue) indicates the target pointing accuracy (\leq 3°).

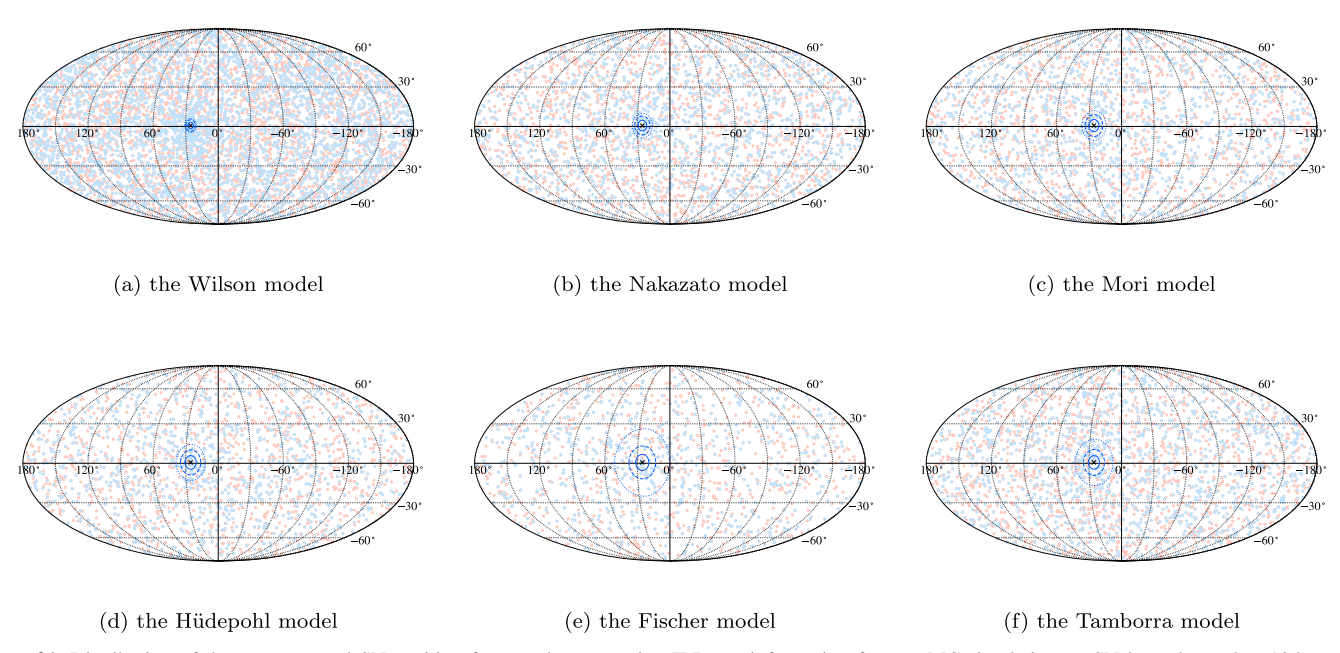


Figure 21. Distribution of the reconstructed SN position from each event using IBD tag information for one MC simulating an SN burst located at 10 kpc with neutrino oscillation in NMO. The light-red points represent the reconstructed SN positions from the IBD-like events, and the light-blue points stand for the reconstructed SN positions from the ES-like events. For each sky map, pointing accuracies at 1σ , 2σ , and 3σ are shown as solid, dashed, and dotted contours in blue, respectively. The black cross at the center of the contour circles represents the true SN position that is arbitrarily selected as R.A. = $1^h41^m43^s$.6, decl. = $0^\circ39'12.5''$.

and where $\hat{d}_{\rm SN}^{\rm true}$ and $\hat{d}_{\rm SN}^{\rm reco}$ are described in Section 3.3. The pointing accuracy at 1σ is then defined as the value of $\Delta\theta$ at which the integral of this distribution contains 68% of the 1000 MC samples when integrating from zero. Figure 20 shows the distribution of $\Delta\theta$ from 1000 simulations of each model and oscillation assumption. Table 6 shows the derived pointing accuracy for the six models, which is seen to vary from $\sim 3^{\circ}$ to $\sim 7^{\circ}$. Although the statistical error is large in some models, it can be seen that the best resolution depends on the oscillation assumption. When neutrino oscillations are considered, better pointing accuracy is achieved in the NMO scenario in the Wilson model, the Nakazato model, and the Fischer model, while in the Mori model, the Hüdepohl model, and the Tamborra models, better pointing is achieved in the IMO scenario.

Figure 21 shows the distribution of the reconstructed SN position from each event using IBD tag information for each model for one MC simulating an SN burst located at 10 kpc with neutrino oscillation in NMO. For each sky map, pointing accuracies at 1σ , 2σ , and 3σ are overlaid as contours in blue. While the reconstructed SN positions from the IBD-like events (pink points) are uniformly distributed, the ES-like events (light-blue points) are concentrated around the true SN position represented as a black cross. The density of each sky map is in proportion to the number of events in the model, and the contour size corresponds to the pointing accuracy of the model.

7. Conclusion and Prospects

Super-Kamiokande plays a crucial role in multimessenger observations of upcoming Galactic SNe by serving as an SN neutrino detector capable of determining the SN direction. With enhanced ability to determine the SN direction following the detector upgrade in 2020 (SK-Gd), we have improved SK's real-time SN monitoring system, SNWATCH (Abe et al. 2016b), and launched the SN warning system, SK_SN Notice. To evaluate the performance of the current SNWATCH, we have investigated SK's response to an SN burst located at a distance of 10 kpc simulated with neutrino fluxes from six SN models.

The studies described above indicate that the response of SK accurately reflects time and energy differences among the SN models that can be used to discriminate between them in the event of an SN burst. Further, using the Gd-loaded detector we have demonstrated the capabilities of IBD tagging on this discrimination and on determining the direction to an SN burst. For example, for the simulation using the Nakazato model with a $20M_{\odot}$, Z=0.02 progenitor, SNWATCH identifies IBD events with an efficiency of $46.86\% \pm 0.04\%$ and results in a sample with $98.82\% \pm 0.01\%$ purity after IBD tagging. Separating into IBD-like and ES-like samples, SNWATCH achieves a pointing accuracy ranging from 3° to 7°, depending upon the SN model.

In order to facilitate follow-up observations using optical telescopes with large fields of view, SK-Gd was designed to achieve a 3° precision using the Wilson model. This has been demonstrated successfully above and marks an improvement of about 20% compared to our previous study. Given that this 3° accuracy has not been attained in other models due to their lower neutrino fluxes, further improvements to SNWATCH are planned. Going forward it will be important to further quantify SK-Gd's ability to distinguish among models and to determine

its ability to extract features of the progenitor from the neutrino data.

Acknowledgments

We gratefully acknowledge the cooperation of the Kamioka Mining and Smelting Company. The Super-Kamiokande experiment has been built and operated from funding by the Japanese Ministry of Education, Culture, Sports, Science and Technology, the U.S. Department of Energy, and the U.S. National Science Foundation. Some of us have been supported by funds from the National Research Foundation of Korea (NRF-2009-0083526 and NRF 2022R1A5A1030700) funded by the Ministry of Science, ICT, the Institute for Basic Science (IBS-R016-Y2), and the Ministry of Education (2018R1D1A1B07049158, 2021R1I1A1A01042256, 2021R1I1A1A01059559), the Japan Society for the Promotion of Science, the National Natural Science Foundation of China under grant No. 11620101004, the Spanish Ministry of Science, Universities and Innovation (grant PGC2018-099388-B-I00), the Natural Sciences and Engineering Research Council (NSERC) of Canada, the Scinet and Westgrid consortia of Compute Canada, the National Science Centre (UMO-2018/30/ E/ST2/00441 and UMO-2022/46/E/ST2/00336) and the Ministry of Science and Higher Education (2023/WK/04), Poland, the Science and Technology Facilities Council (STFC) and GridPPP, UK, the European Union's Horizon 2020 Research and Innovation Programme under the Marie Sklodowska-Curie grant agreement No. 754496, H2020-MSCA-RISE-2018 JENNIFER2 grant agreement No. 822070, and H2020-MSCA-RISE-2019 SK2HK grant agreement No.

Software: ROOT (Brun & Rademakers 1997), matplotlib (Hunter 2007), NumPy (van der Walt et al. 2011), SciPy (Virtanen et al. 2020), astropy (Astropy Collaboration et al. 2013, 2018), Cloudy (Ferland et al. 2013), Source Extractor (Bertin & Arnouts 1996).

Appendix A Data Format Unification

SKSNSim has a class to read "Nakazato format" in which the differential neutrino flux $\Delta N_{k,\nu_i}(t_n)/\Delta E_k$ and differential neutrino luminosity $\Delta L_{k,\nu_i}(t_n)/\Delta E_k$ at the time t_n are provided for each neutrino flavor ν_i ($i=e,\mu,\tau$) and energy bin E_k as described in the Appendix of Nakazato et al. (2013).⁶⁴ We prepared the lists of time–luminosity pairs $(t,L_{\nu_i}(t))$ and time–mean energy pairs $(t,\langle E_{\nu_i}\rangle(t))$ by scanning the plots of the time evolution of luminosity and mean energy in the published papers. How this "data format unification" is conducted is described below.

A.1. Linear Interpolation and Extrapolation

Besides the Nakazato model, the Mori model is provided in "Nakazato format" with slightly different energy binning E_k . Other non "Nakazato format" models (the Wilson model, the Hüdepohl model, the Fischer model, and the Tamborra model) need data format unification. For these four models, we used the same energy binning as that of the Nakazato model. For the Hüdepohl model, the lists of $(t, L_{\nu_k}(t))$ pairs and $(t, \langle E_{\nu_k} \rangle(t))$

⁶⁴ The "Nakazato format" data of Nakazato et al. (2013) and their guide are available on the website http://asphwww.ph.noda.tus.ac.jp/snn/.

pairs are already provided in the repository of the SK database.65 Regarding the Wilson model and the Fischer model, we scanned the figures of luminosity versus time and mean energy versus time using a web-based plot digitizing tool WebPlotDigitizer (Rohatgi 2022) for each neutrino flavor to make the lists of $(t, L_{\nu_i}(t))$ and $(t, \langle E_{\nu_i} \rangle(t))$. Since the time data points t of these three models are not identical among neutrino flavors ν_i , we performed linear interpolations and extrapolations to each list before making them into "Nakazato format" (described in the following Sections A.2–A.3).

Note that the Fischer model's ν_e luminosity curve (the upperleft panel of Figure 2 in Fischer et al. 2010) starts later than that of other flavors, which requires extrapolation of ν_e luminosity so that it has the same time range as the other flavors' luminosity data points. Since the maximum luminosity and the rising edge of $\nu_{\rm e}$ luminosity is out of the plotted region, linear extrapolation is the only possible way to realize this. For the Tamborra model, we took advantage of SNEWPY (Baxter et al. $(2022)^{66}$ that has the lists of $(t, L_{\nu_i}(t))$ and $(t, \langle E_{\nu_i} \rangle(t))$ with the identical time data points among flavors.

A.2. Differential Neutrino Flux Calculation

The goal of this "data format unification" is to obtain the differential neutrino flux $\Delta N_{k,\nu_i}(t_n)/\Delta E_k$ (s⁻¹MeV⁻¹) and differential neutrino luminosity $\Delta L_{k,\nu_i}(t_n)/\Delta E_k$ (erg s⁻¹MeV⁻¹) at the time $t_n(s)$ for each neutrino flavor ν_i ($i = e, \mu, \tau$) and energy bin E_k from the available pairs of $(t, L_{\nu_k}(t))$ and $(t, \langle E_{\nu_i} \rangle(t))$. The time-integrated flux of SN neutrino (MeV⁻¹ kpc⁻²) is represented as

$$\frac{\mathrm{d}F(E_{\nu})}{\mathrm{d}E_{\nu}} = \frac{1}{4\pi d_{\mathrm{SN}}^2} \frac{E_{\nu_{i},\mathrm{total}}}{\langle E_{\nu_{i}} \rangle} f(E_{\nu}). \tag{A1}$$

where d_{SN} (kpc) is the distance to the SN, $E_{\nu,total}$ (MeV) represents the total energy emitted by ν_i , $\langle E_{\nu_i} \rangle$ (MeV) stands for the average energy of ν_i , and $f(E_{\nu})$ is a normalized distribution function (Nakazato et al. 2018). Since SKSNSim calculates the distance term $1/4\pi d_{SN}^2$, it does not need to be considered here. As $f(E_{\nu})$, we assume a Fermi–Dirac distribution

$$f_{\rm FD}(E_{\nu}) = \frac{2}{3\zeta(3)T_{\nu_i}^3} \frac{E_{\nu}^2}{e^{E_{\nu}/T_{\nu_i}} + 1} \tag{A2}$$

where $\zeta(3) \approx 1.202$ is the zeta function and

$$T_{\nu_i} = \frac{180}{7\pi^4} \zeta(3) \langle E_{\nu_i} \rangle \approx \frac{\langle E_{\nu_i} \rangle}{3.151} \tag{A3}$$

is the neutrino temperature in the units of MeV. By replacing the total energy $E_{\nu_i,\text{total}}$ (MeV) with the luminosity $L_{\nu_i}(t)$ (erg s⁻¹) and substituting $\langle E_{\nu_i} \rangle = \langle E_{\nu_i} \rangle (t)$ in Equations (A1)– (A3), the expression of the differential neutrino flux $(s^{-1}MeV^{-1})$ is obtained as

$$\frac{\mathrm{d}^2 N_{\nu}}{\mathrm{d}E_{\nu}\mathrm{d}t} = \frac{L_{\nu_i}(t)}{\langle E_{\nu_{\nu}}\rangle(t)} \frac{2}{3\zeta(3)T_{\nu_i}^3} \frac{E_{\nu}^2}{e^{E_{\nu}/T_{\nu_i}} + 1} \tag{A4}$$

where $T_{\nu_i} \approx \langle E_{\nu_i} \rangle (t) / 3.151$ (MeV).

The differential neutrino luminosity (erg s⁻¹ MeV⁻¹) can be computed from the differential neutrino flux (s⁻¹ MeV⁻¹) as

$$\frac{\Delta L_{k,\nu_i}(t_n)}{\Delta E_{\nu}} = \frac{\Delta N_{k,\nu_i}(t_n)}{\Delta E_{\nu}} \times E_k \times \frac{1.6022 \times 10^{-6} \text{erg}}{\text{MeV}} \quad (A5)$$

A.3. Normalization for Reproducing Original Luminosity

In order to reproduce the original luminosity versus time plot and mean energy versus time plot from the "Nakazato format" table, a normalization factor is necessary. Such normalization factor is written as

Normalizing Factor at
$$t = \frac{\text{original luminosity at } t}{\text{reproduced luminosity at } t}$$
, (A6)

where the original luminosity is $L_{\nu_i}(t)$ provided in the list and the reconstructed luminosity $L_{\nu_i, \text{reco}}(t)$ is obtained by the energy-integration of the differential neutrino luminosity as

$$L_{\nu_i, \text{reco}}(t) = \sum_{k} \frac{\Delta L_{k, \nu_i}(t)}{\Delta E_k} \times (E_{k+1} - E_k). \tag{A7}$$

By multiplying Equation (A6) by the results Equations (A4)-(A5) and arranging them, the normalized "Nakazato format" tables of other models are obtained.

Appendix B Comparison of SK-Gd's Response among Models for Supernova at 10 kpc

This Appendix contains figures showing comparison of SK-Gd's response among models for an SN burst located at 10 kpc with neutrino oscillation in the NMO and IMO scenarios, which could not be included in Section 5. We note again that reconstructed events in the following figures correspond to events after reconstruction in SNWATCH in Figure 3 and after the time matching between the reconstructed time and the generated time by SKSNSim described in Section 5. Figure 22 shows the comparison of time evolution of the number of events up to 20 s among interactions for each model in the NMO scenario (top six panels) and the IMO scenario (bottom six panels). Figures 23 and 24 show the same as Figure 22 but up to 1.5 s and 0.12 s, respectively. From Figure 23, we can see significant differences in the time structure of ES events (green) and ¹⁶O CC events (blue); in the Mori model (top-right panel in Figure 23), the ES events excess over ¹⁶OCC events is observed at 0 s, which corresponds to the neutronization burst mentioned in Section 5.2. The ES excess over ¹⁶O CC is seen in all the models other than the Nakazato model. In the Nakazato model, characterized by the large number of ¹⁶O CC events within the first 0.25 s as shown in the top-middle panel in Figure 23, the yield of ¹⁶O CC events exceeds the number of ES events. The time structure of the Wilson model regarding ¹⁶O CC is characterized by the long-lasting ¹⁶O CC events excess over the ES events. These excesses of ¹⁶O CC events over ES events are caused by the larger cross section of ¹⁶O CC interaction in higher-energy regions (shown in Figure 2). The Tamborra model has a similar characteristic to this; however, it differs from the other five models in the feature of an increasing number of events after the first neutrino emission peak; the number of events in the other models attenuates after the first neutrino emission peak. Figure 25 shows comparison of time evolution of events among models for each interaction covering

⁶⁵ Prepared for developing SNWATCH. The data are confirmed to reproduce the published plots.

66 Available on the GitHub https://github.com/SNEWS2/snewpy.

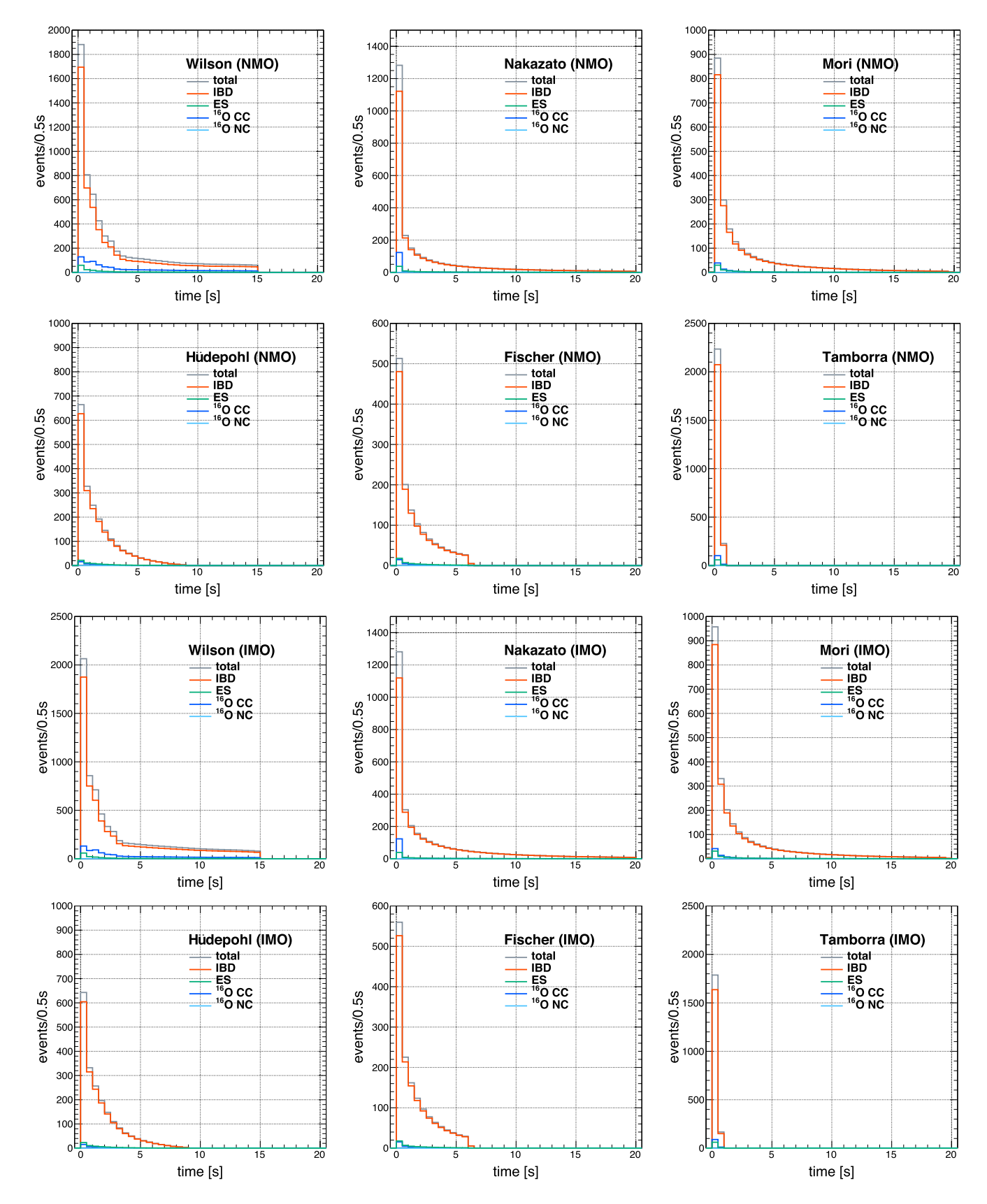


Figure 22. Comparison of time evolution up to 20 s among interactions for each model for an SN burst located at 10 kpc in the NMO scenario (top six panels) and the IMO scenario (bottom six panels).

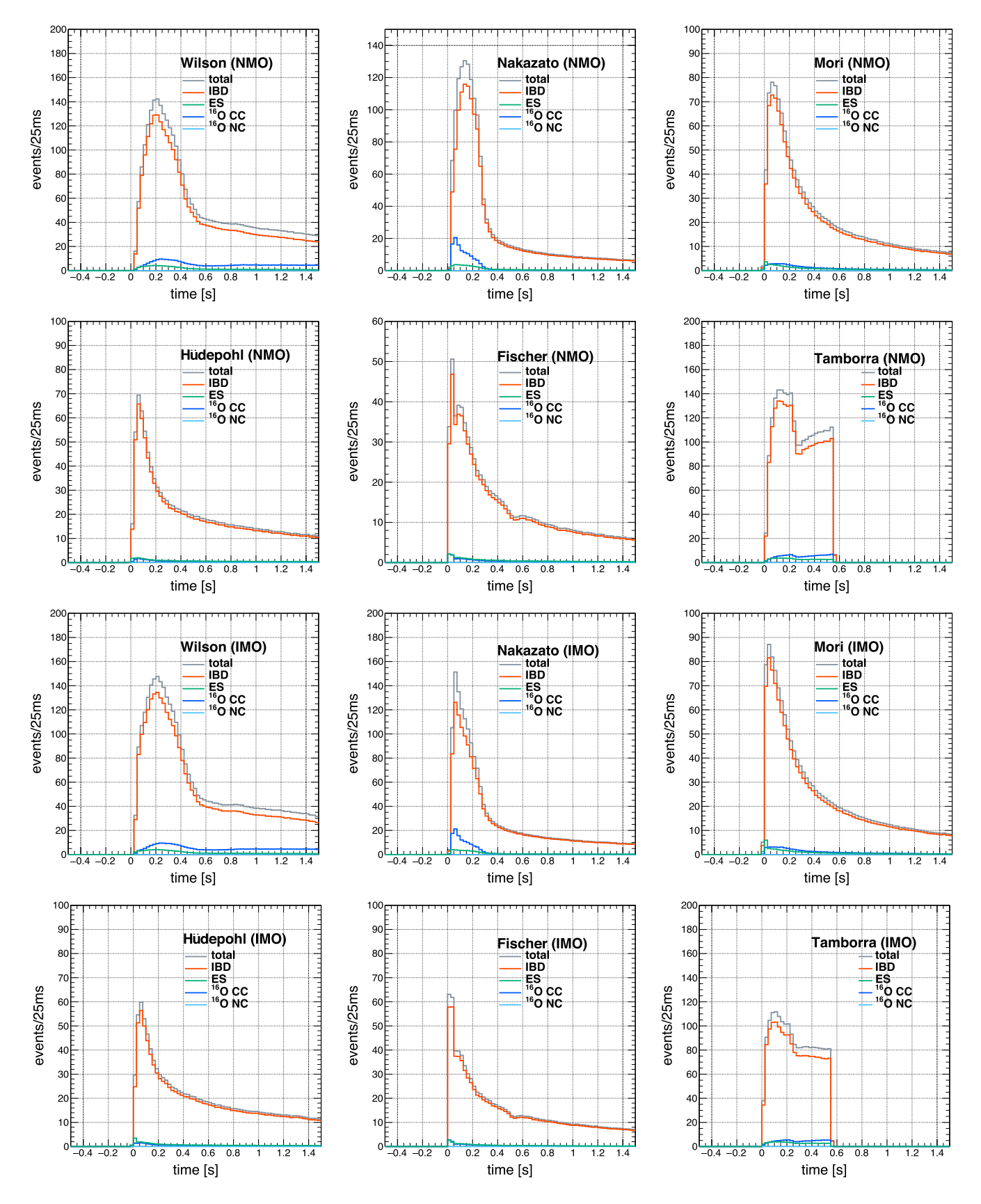


Figure 23. Comparison of time evolution up to 1.5 s among interactions for each model for an SN burst located at 10 kpc in the NMO scenario (top six panels) and the IMO scenario (bottom six panels).

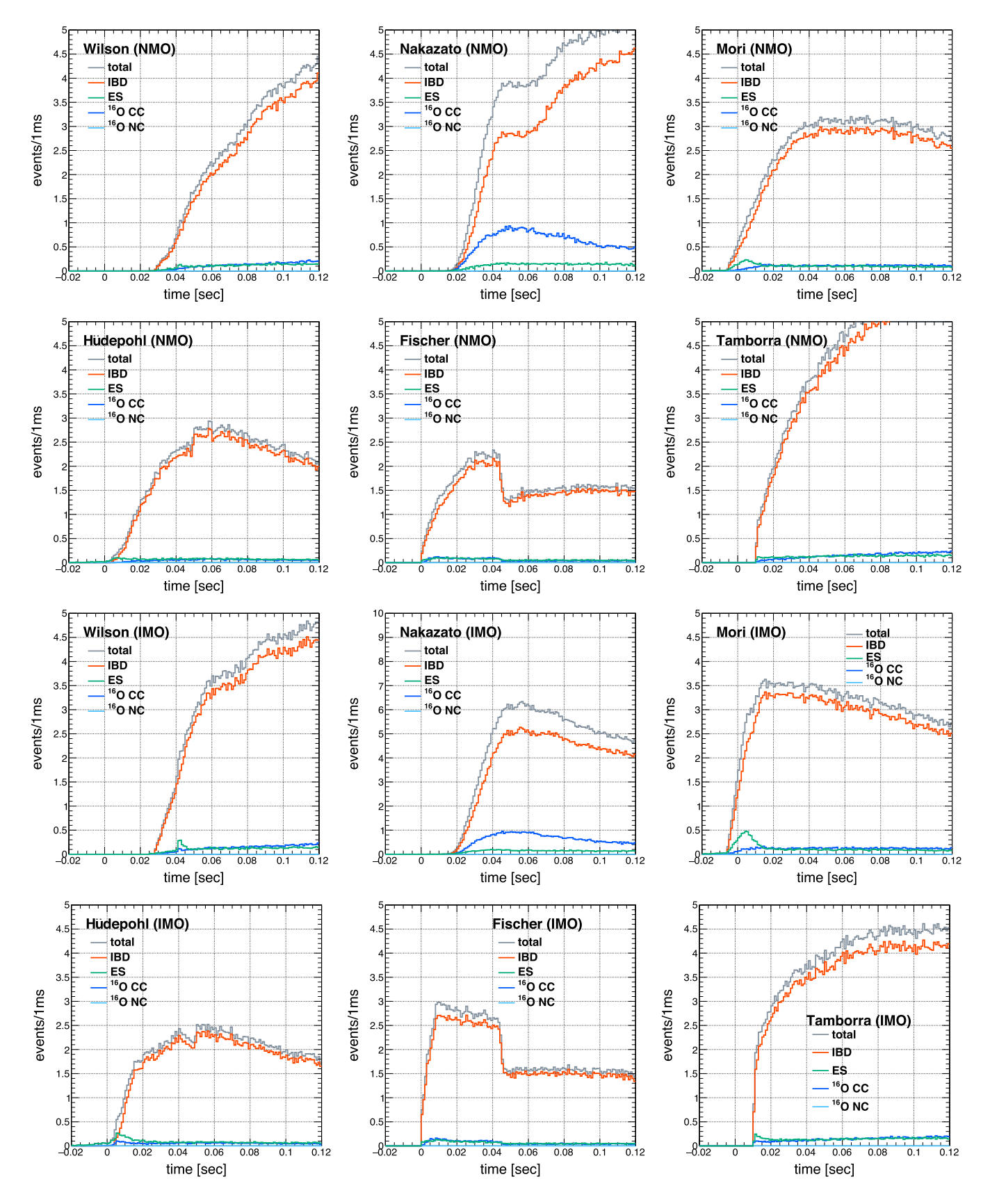


Figure 24. Comparison of time evolution up to 0.12 s among interactions for each model for an SN burst located at 10 kpc in the NMO scenario (top six panels) and the IMO scenario (bottom six panels).

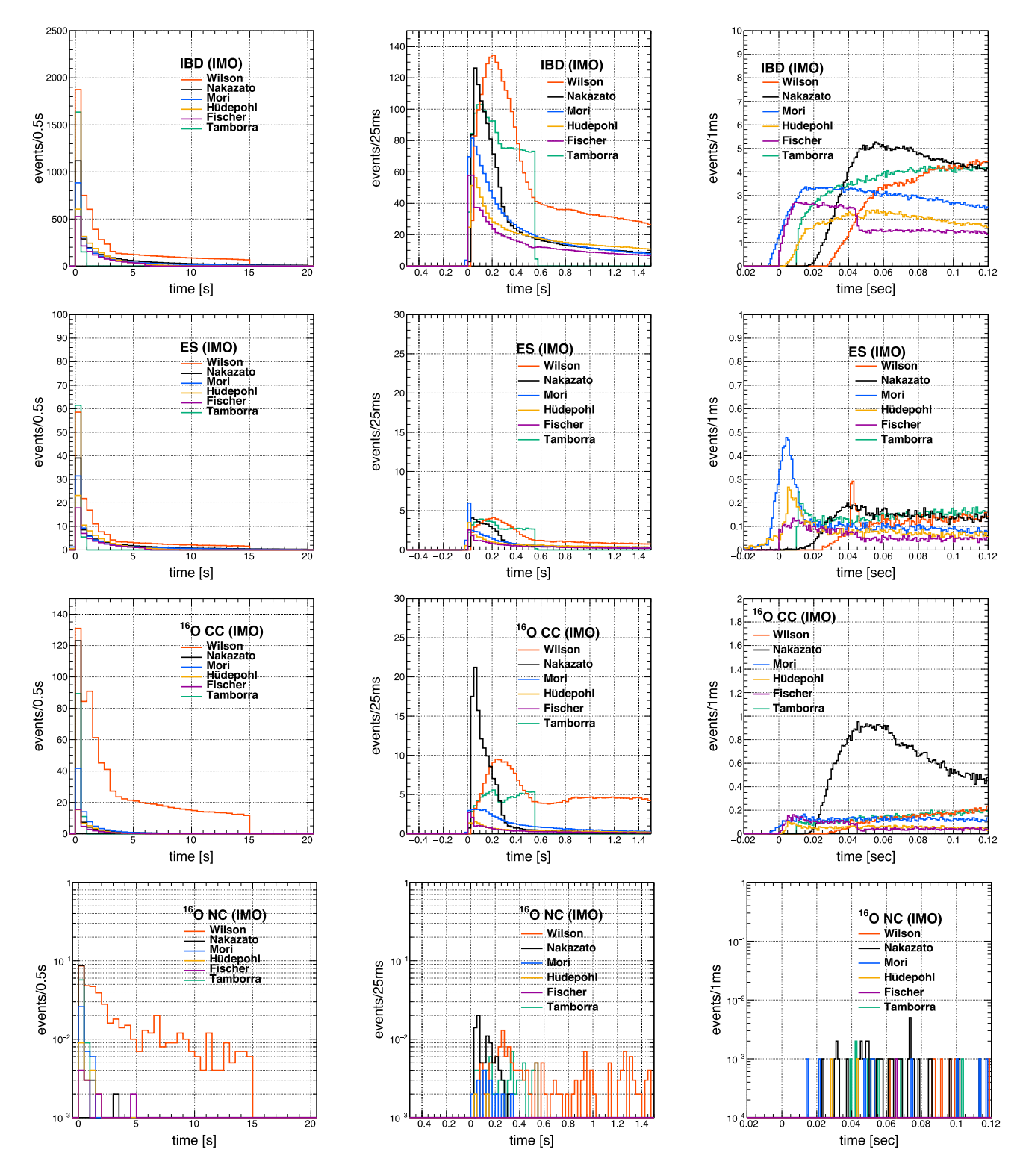


Figure 25. Comparison of time evolution among models for each interaction for an SN burst located at 10 kpc in neutrino oscillation with IMO. The left, middle, and right columns show the time evolution up to 0.12 s, 1.5 s, and 20 s, respectively. Each row represents IBD, ES, ^{16}O CC, and ^{16}O NC from top to bottom.

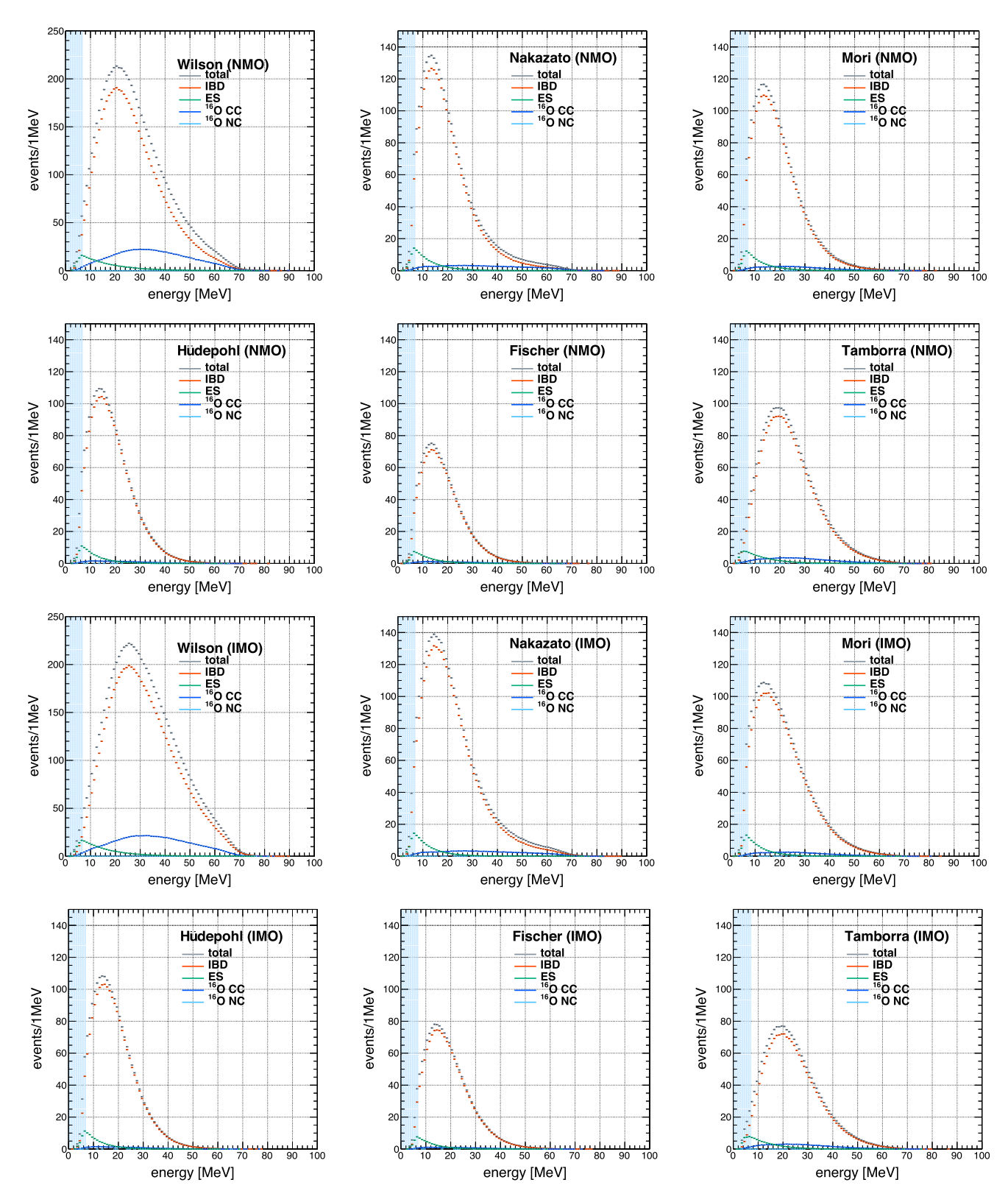


Figure 26. Comparison of energy spectra among interactions for each model in the IMO scenario. The energy region below the 7 MeV threshold for selecting "prompt" candidates is shaded in light blue.

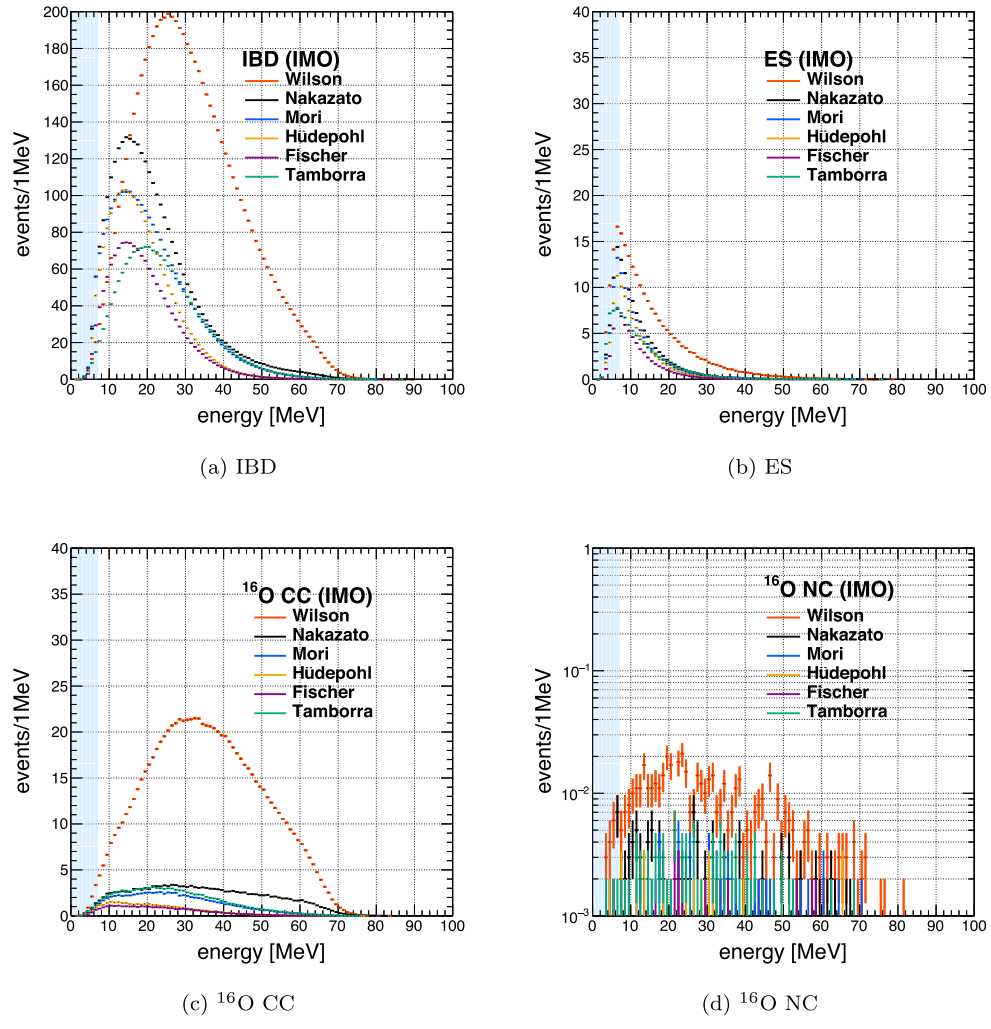


Figure 27. Comparison of energy spectra among models for each interaction for an SN located at 10 kpc in the IMO scenario: (a) IBD, (b) ES, (c) ^{16}O CC, and (d) ^{16}O NC. The energy region below the 7 MeV threshold for selecting "prompt" candidates is shaded in light blue.

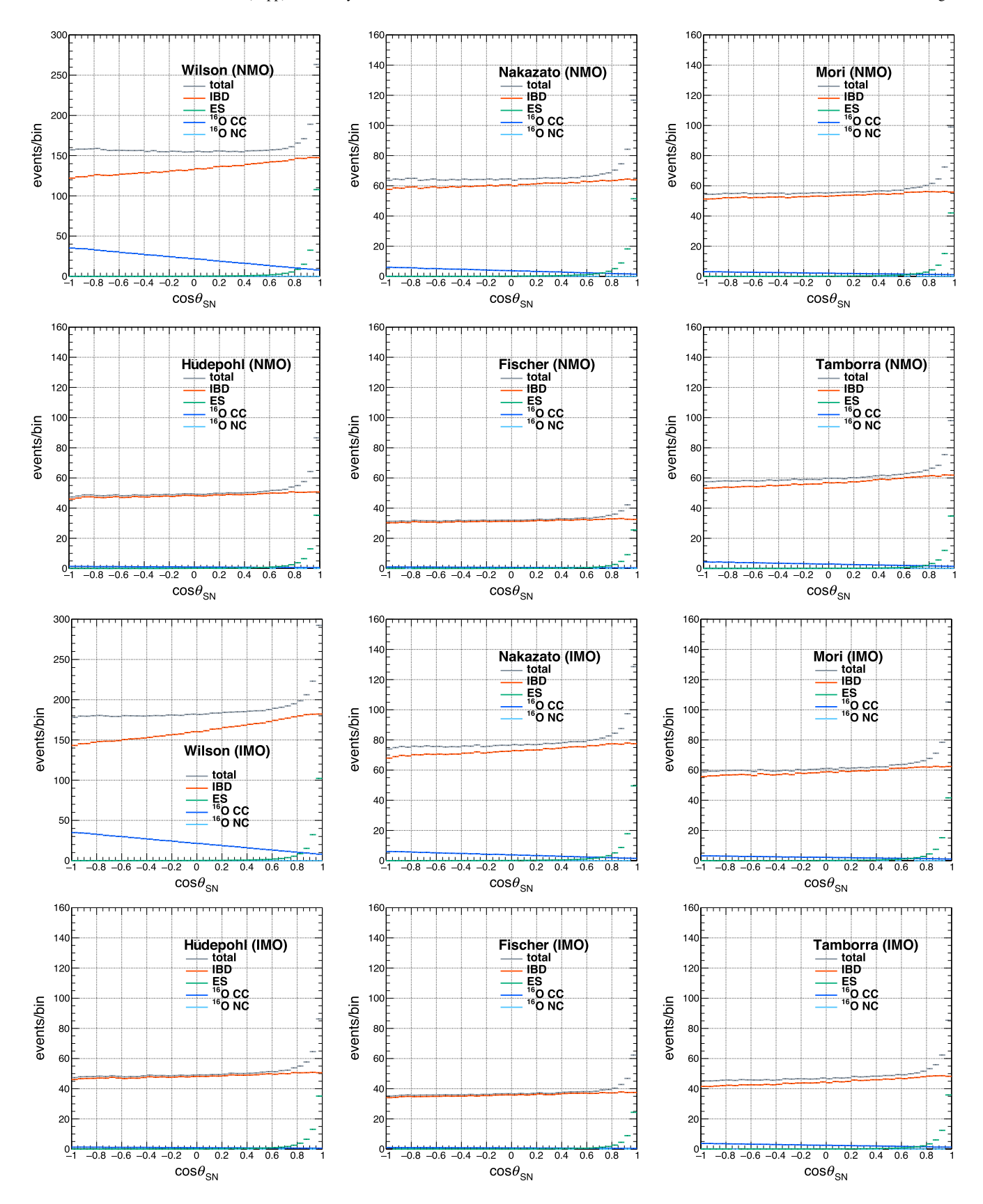


Figure 28. Comparison of $\cos \theta_{\rm SN}$ distribution among interactions for each model for an SN burst located at 10 kpc in the NMO scenario (top six panels) and the IMO scenario (bottom six panels).

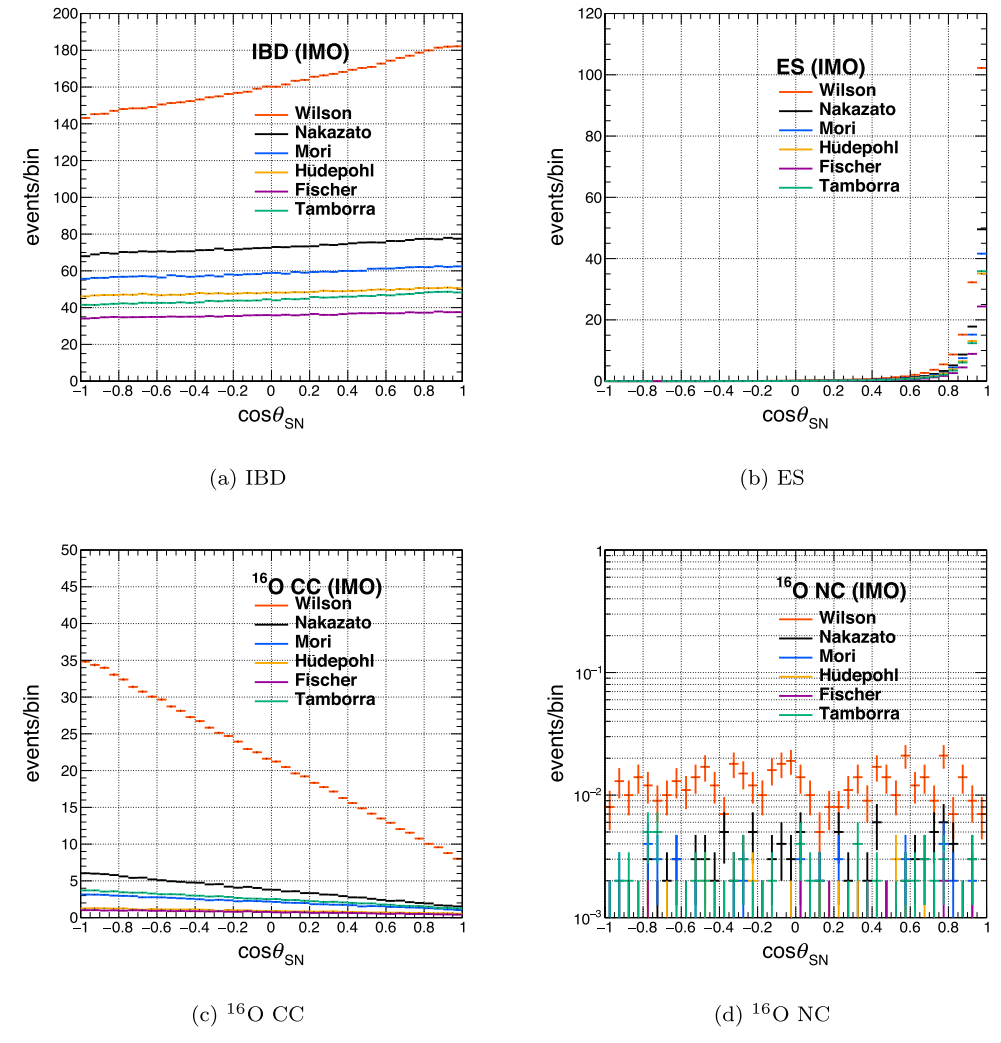


Figure 29. Comparison of $\cos \theta_{\rm SN}$ distribution among models for each interaction for SN at 10 kpc in the IMO scenario: (a) IBD, (b) ES, (c) 16 O CC, and (d) 16 O NC.

three different time ranges in the IMO scenario, similar to Figure 12. The peaks due to the neutronization burst are stronger than those observed in Figure 12; they are also observed in the Hüdepohl model (orange), slightly in the Nakazato model (black) and the Fischer model (purple), as well as for the Mori model (blue) and the Wilson model (red). Note that the reconstructed events in Figures 22–25 satisfy the same event selection described in Section 3.1.

Figure 26 shows the energy spectra among interactions for each model in the NMO scenario (top six panels) and the IMO scenario (bottom six panels). It is obviously seen that the energy contribution from IBD events is dominant for all models. Comparison of energy spectra among models in the IMO scenario is shown in Figure 27, similar to Figure 13. Note that the reconstructed events in Figures 26–27 satisfy the same event selection described in Section 3.1 except for the energy condition.

Figure 28 shows the $\cos\theta_{\rm SN}$ distribution of each interaction for each model for an SN burst located at 10 kpc in the NMO scenario (top six panels) and the IMO scenario (bottom six panels). Comparison of angular distribution of events among models for each interaction for an SN burst located at 10 kpc is shown in Figure 29, similar to Figure 14. Note that the reconstructed events in Figures 28–29 satisfy the same event selection described in Section 3.1.

ORCID iDs

Y. Kashiwagi https://orcid.org/0000-0002-3926-8333

C. Bronner https://orcid.org/0000-0001-9555-6033 Y. Hayato https://orcid.org/0000-0002-8683-5038 K. Hiraide https://orcid.org/0000-0003-1229-9452 K. Hosokawa https://orcid.org/0000-0002-8766-3629 K. Ieki https://orcid.org/0000-0002-7791-5044 M. Ikeda https://orcid.org/0000-0002-4177-5828 Y. Kataoka https://orcid.org/0000-0001-9090-4801 S. Moriyama https://orcid.org/0000-0001-7630-2839 Y. Nakano https://orcid.org/0000-0003-1572-3888 M. Nakahata https://orcid.org/0000-0001-7783-9080 S. Nakayama https://orcid.org/0000-0002-9145-714X Y. Noguchi https://orcid.org/0000-0002-3113-3127 H. Sekiya https://orcid.org/0000-0001-9034-0436 M. Shiozawa https://orcid.org/0000-0003-0520-3520 Y. Takemoto https://orcid.org/0000-0003-2232-7277 T. Yano https://orcid.org/0000-0002-5320-1709 K. Okumura https://orcid.org/0000-0002-5523-2808 T. Tashiro https://orcid.org/0000-0003-1440-3049 P. Fernandez https://orcid.org/0000-0001-9034-1930 L. Labarga https://orcid.org/0000-0002-6395-9142 N. Ospina https://orcid.org/0000-0002-8404-1808 E. Kearns https://orcid.org/0000-0002-1781-150X

```
L. Wan https://orcid.org/0000-0001-5524-6137
T. Wester https://orcid.org/0000-0001-6668-7595
N. J. Griskevich https://orcid.org/0000-0003-4409-3184
H. W. Sobel https://orcid.org/0000-0001-5073-4043
A. Yankelevich https://orcid.org/0000-0002-5963-3123
B. Bodur https://orcid.org/0000-0001-8454-271X
K. Scholberg https://orcid.org/0000-0002-7007-2021
C. W. Walter https://orcid.org/0000-0003-2035-2380
Th. A. Mueller https://orcid.org/0000-0003-2743-4741
P. Paganini https://orcid.org/0000-0001-9580-683X
R. Rogly https://orcid.org/0000-0003-2530-5217
L. N. Machado https://orcid.org/0000-0002-7578-4183
N. Iovine https://orcid.org/0000-0001-7965-2252
N. W. Prouse https://orcid.org/0000-0003-1037-3081
M. Scott https://orcid.org/0000-0002-1759-4453
V. Berardi  https://orcid.org/0000-0002-8387-4568
N. F. Calabria https://orcid.org/0000-0003-3590-2808
A. Langella https://orcid.org/0000-0001-6273-3558
G. Collazuol https://orcid.org/0000-0002-7876-6124
F. Iacob https://orcid.org/0000-0003-3582-3819
M. Mattiazzi  https://orcid.org/0000-0003-3900-6816
L. Périssé https://orcid.org/0000-0003-3444-4454
G. Pronost https://orcid.org/0000-0001-6429-5387
Y. Nishimura https://orcid.org/0000-0002-7666-3789
T. Hasegawa https://orcid.org/0000-0002-2967-1954
T. Matsubara https://orcid.org/0000-0003-3187-6710
Y. Oyama https://orcid.org/0000-0002-1689-0285
F. Di Lodovico https://orcid.org/0000-0003-3952-2175
T. Katori https://orcid.org/0000-0002-9429-9482
J. Migenda https://orcid.org/0000-0002-5350-8049
R. M. Ramsden https://orcid.org/0009-0005-3298-6593
S. Zsoldos https://orcid.org/0000-0003-0142-4844
Y. Takeuchi https://orcid.org/0000-0002-4665-2210
J. R. Hu https://orcid.org/0000-0003-2149-9691
Z. Hu https://orcid.org/0000-0002-0353-8792
T. Nakaya https://orcid.org/0000-0003-3040-4674
R. A. Wendell https://orcid.org/0000-0002-0969-4681
S. J. Jenkins https://orcid.org/0000-0002-0982-8141
N. McCauley https://orcid.org/0000-0002-5982-5125
A. Tarrant https://orcid.org/0000-0002-8750-4759
Y. Fukuda https://orcid.org/0000-0003-2660-1958
Y. Itow https://orcid.org/0000-0002-8198-1968
H. Menjo https://orcid.org/0000-0001-8466-1938
C. Yanagisawa https://orcid.org/0000-0002-6490-1743
M. Harada https://orcid.org/0000-0003-3273-946X
Y. Hino https://orcid.org/0000-0002-7480-463X
Y. Koshio https://orcid.org/0000-0003-0437-8505
F. Nakanishi https://orcid.org/0000-0003-4408-6929
S. Sakai https://orcid.org/0000-0002-2190-0062
D. Barrow https://orcid.org/0000-0001-5844-709X
F. Nova https://orcid.org/0000-0002-0769-9921
S. Jung https://orcid.org/0009-0007-8244-8106
B. S. Yang https://orcid.org/0000-0001-5877-6096
J. Y. Yang https://orcid.org/0000-0002-3624-3659
L. Kneale https://orcid.org/0000-0002-4087-1244
M. D. Thiesse https://orcid.org/0000-0002-0775-250X
L. F. Thompson https://orcid.org/0000-0001-6911-4776
E. Kwon https://orcid.org/0000-0001-5653-2880
J. W. Seo https://orcid.org/0000-0002-2719-2079
I. Yu https://orcid.org/0000-0003-1567-5548
K. D. Nakamura https://orcid.org/0000-0003-3302-7325
S. Tairafune https://orcid.org/0000-0002-2140-7171
K. Nishijima https://orcid.org/0000-0002-1830-4251
```

Y. Nakajima https://orcid.org/0000-0002-2744-5216 M. Yokoyama https://orcid.org/0000-0003-2742-0251 P. de Perio https://orcid.org/0000-0002-0741-4471 S. Fujita https://orcid.org/0000-0002-0281-2243 C. Jesús-Valls https://orcid.org/0000-0002-0154-2456 M. R. Vagins https://orcid.org/0000-0002-0569-0480 J. Xia https://orcid.org/0000-0003-1412-092X M. Kuze https://orcid.org/0000-0001-8858-8440 S. Izumiyama https://orcid.org/0000-0002-0808-8022 R. Matsumoto https://orcid.org/0000-0002-4995-9242 H. Ito https://orcid.org/0000-0003-1029-5730 M. Shinoki https://orcid.org/0000-0002-9486-6256 K. Yamauchi https://orcid.org/0009-0000-0112-0619 B. D. Xu https://orcid.org/0000-0001-5135-1319 B. Zhang https://orcid.org/0000-0001-7832-2972 M. Posiadala-Zezula https://orcid.org/0000-0002-5154-5348 Ll. Marti https://orcid.org/0000-0002-5172-9796 A. Minamino https://orcid.org/0000-0001-6510-7106

References

```
Abe, K., Adrich, P., Aihara, H., et al. 2021, ApJ, 916, 15
Abe, K., Bronner, C., Hayato, Y., et al. 2022a, NIMPA, 1027, 166248
Abe, K., Bronner, C., Hayato, Y., et al. 2022b, APh, 139, 102702
Abe, K., Bronner, C., Hayato, Y., et al. 2024, NIMPA, 1065, 169480
Abe, K., Haga, Y., Hayato, Y., et al. 2016a, PhRvD, 94, 052010
Abe, K., Haga, Y., Hayato, Y., et al. 2016b, APh, 81, 39
Alexeyev, E., Alexeyeva, L., Krivosheina, I., & Volchenko, V. 1988, PhLB,
Antonioli, P., Fienberg, R. T., Fleurot, F., et al. 2004, NJPh, 6, 114
Astropy Collaboration, Price-Whelan, A. M., Sipőcz, B. M., et al. 2018, AJ,
   156, 123
Astropy Collaboration, Robitaille, T. P., Tollerud, E. J., et al. 2013, A&A,
   558, A33
Bahcall, J. N., Kamionkowski, M., & Sirlin, A. 1995, PhRvD, 51, 6146
Barthelmy, S. D., Cline, T., Butterworth, P., et al. 2000, in AIP Conf. Proc.
   526, Gamma-Ray Bursts: 5th Huntsville Symposium (Melville, NY:
   AIP), 731
Baxter, A. L., BenZvi, S., Jaimes, J. C., et al. 2022, ApJ, 925, 107
Beacom, J. F., & Vagins, M. R. 2004, PhRvL, 93, 171101
Bertin, E., & Arnouts, S. 1996, A&AS, 117, 393
Bethe, H. A., & Wilson, J. R. 1985, ApJ, 295, 14
Bionta, R. M., Blewitt, G., Bratton, C. B., et al. 1987, PhRvL, 58, 1494
Bruenn, S. W. 1985, ApJS, 58, 771
Brun, R., & Rademakers, F. 1997, NIMPA, 389, 81
Buras, R., Rampp, M., Janka, H.-T., & Kifonidis, K. 2006, A&A, 447, 1049
Burrows, A. 2013, Rev. Mod. Phys., 85, 245
Burrows, A., Livne, E., Dessart, L., Ott, C., & Murphy, J. 2006, ApJ, 640, 878
Dighe, A. S., & Smirnov, A. Y. 2000, PhRvD, 62, 033007
Ferland, G. J., Porter, R. L., van Hoof, P. A. M., et al. 2013, RMxAA, 49, 137
Fischer, T., Whitehouse, S., Mezzacappa, A., Thielemann, F.-K., &
   Liebendoerfer, M. 2010, A&A, 517, A80
Fryxell, B., Mueller, E., & Arnett, D. 1991, ApJ, 367, 619
Fukuda, S., Fukuda, Y., Hayakawa, T., et al. 2003, NIMPA, 501, 418
Hagiwara, K., Yano, T., Tanaka, T., et al. 2019, PTEP, 2019, 023D01
Harada, M. 2020, JPhCS, 1468, 012255
Hempel, M., & Schaffner-Bielich, J. 2010, NuPhA, 837, 210
Herant, M., Benz, W., Hix, W. R., Fryer, C. L., & Colgate, S. A. 1994, ApJ,
   435, 339
Hosaka, J., Ishihara, K., Kameda, J., et al. 2006, PhRvD, 73, 112001
Hüdepohl, L., Müller, B., Janka, H.-T., Marek, A., & Raffelt, G. G. 2010,
   PhRvL, 104, 251101
Hunter, J. D. 2007, CSE, 9, 90
Janka, H. T. 2001, A&A, 368, 527
Kolbe, E., Langanke, K., & Vogel, P. 2002, PhRvD, 66, 013007
Kuroda, T. 2021, ApJ, 906, 128
Langanke, K., Vogel, P., & Kolbe, E. 1996, PhRvL, 76, 2629
Lattimer, J. M., & Swesty, F. D. 1991, NuPhA, 535, 331
Liebendörfer, M., Messer, O. B., Mezzacappa, A., et al. 2004, ApJS, 150, 263
Marek, A., & Janka, H.-T. 2009, ApJ, 694, 664
```

Mayle, R., Wilson, J. R., & Schramm, D. N. 1987, ApJ, 318, 288

Mori, M., Suwa, Y., Nakazato, K., et al. 2021, PTEP, 2021, 023E01

```
Nakamura, K., Horiuchi, S., Tanaka, M., et al. 2016, MNRAS, 461, 3296
Nakanishi, F., Izumiyama, S., Harada, M., & Koshio, Y. 2024, ApJ, 965, 91
Nakazato, K., Sumiyoshi, K., Suzuki, H., et al. 2013, ApJS, 205, 2
Nakazato, K., Suzuki, T., & Sakuda, M. 2018, PTEP, 2018, 123E02
Nishino, H., Awai, K., Hayato, Y., et al. 2007, in IEEE Nuclear Science Symp.
Conf. Record, 1 (Piscataway, NJ: IEEE), 127
Nomoto, K. 1987, ApJ, 322, 206
O'Connor, E. 2015, ApJS, 219, 24
Odrzywolek, A., Misiaszek, M., & Kutschera, M. 2004, AcPPB, 35, 1981
Orii, A. 2015, ICRC (The Hague), 236, 1161
Orii, A., Tomura, T., Hayato, Y., et al. 2014, in 2014 IEEE Nuclear Science Symp. and Medical Imaging Conf. (NSS/MIC) (Piscataway, NJ: IEEE), 1
Particle Data Group, Workman, R., Burkert, V., et al. 2022, PTEP, 2022, 083C01
Rampp, M., & Janka, H.-T. 2002, A&A, 396, 361
Rohatgi, A. 2022, Webplotdigitizer: v4.6, https://automeris.io/WebPlot Digitizer
```

```
Rutledge, R. E. 1998, PASP, 110, 754
Scholberg, K. 2008, AN, 329, 337
Shen, H., Toki, H., Oyamatsu, K., & Sumiyoshi, K. 1998, NuPhA, 637, 435
Shen, H., Toki, H., Oyamatsu, K., & Sumiyoshi, K. 1998, PThPh, 100, 1013
Strumia, A., & Vissani, F. 2003, PhLB, 564, 42
Suzuki, T., Chiba, S., Yoshida, T., Takahashi, K., & Umeda, H. 2018, PhRvC,
  98, 034613
Tamborra, I., Raffelt, G., Hanke, F., Janka, H.-T., & Mueller, B. 2014, PhRvD,
Tanaka, T., Hagiwara, K., Gazzola, E., et al. 2020, PTEP, 2020, 043D02
Tomas, R., Semikoz, D., Raffelt, G. G., Kachelriess, M., & Dighe, A. 2003,
  PhRvD, 68, 093013
Totani, T., Sato, K., Dalhed, H., & Wilson, J. 1998, ApJ, 496, 216
van der Walt, S., Colbert, S. C., & Varoquaux, G. 2011, CSE, 13, 22
Virtanen, P., Gommers, R., Oliphant, T. E., et al. 2020, NatMe, 17, 261
Wilson, J., Mayle, R., Woosley, S., & Weaver, T. 1986, NYASA, 470, 267
Woosley, S. E., Heger, A., & Weaver, T. A. 2002, RevMP, 74, 1015
```